

Balancing truncation and round-off errors in practical FEM: one-dimensional analysis

Jie Liu^{a,*}, Matthias Möller^a, Henk M. Schuttelaars^a

^a*Delft Institute of Applied Mathematics
Delft University of Technology*

Van Mourik Broekmanweg 6, 2628 XE Delft, The Netherlands

5

Abstract

In finite element methods (FEMs), the accuracy of the solution cannot increase indefinitely because the round-off error increases when the number of degrees of freedom (DoFs) is large enough. This means that the accuracy that can be reached is limited. A priori information of the highest attainable accuracy is therefore of great interest. In this paper, we devise an innovative method to obtain the highest attainable accuracy. In this method, the truncation error is extrapolated when it converges at the analytical rate, for which only a few primary h -refinements are required, and the bound of the round-off error is provided through extensive numerical experiments. The highest attainable accuracy is obtained by minimizing the sum of these two types of errors. We validate this method using a one-dimensional Helmholtz equation in space. It shows that the highest attainable accuracy can be accurately predicted, and the CPU time required is much less compared with that using the successive h -refinement.

Keywords: Finite Element Method (FEM), error estimation, optimal number of degrees of freedom, hp -refinement strategy.

1. Introduction

Many problems in engineering sciences and industry are modelled mathematically by initial-boundary value problems comprising systems of coupled, nonlinear partial and/or ordinary differential equations. These problems often consider complex geometries, with initial and/or boundary conditions that depend on measured data [1]. In some applications, not only the solution, but also its derivatives are of interest [1, 2]. For many problems of practical interest, analytical or semi-analytical solutions are not available, and hence one has to resort to numerical solution methods, such as the finite difference, finite volume, and finite element methods. The latter will be adopted throughout this paper and applied to one-dimensional boundary value problems.

*Corresponding author

Email addresses: j.liu-5@tudelft.nl (Jie Liu), m.moller@tudelft.nl (Matthias Möller), h.m.schuttelaars@tudelft.nl (Henk M. Schuttelaars)

The accuracy of the numerically obtained solution is influenced by many sources of errors [3]: firstly, errors in the set-up of the models, such as the simplification of the domain and governing equations and the approximation of the initial and boundary conditions; next, truncation errors due to the discretization of the computational domain and the use of basis functions for the function spaces defined on it; then, the iteration error resulting from the artificially controlled tolerance of iterative solvers; finally, the round-off error due to the adoption of finite-precision computer arithmetics, rather than exact arithmetics. One tacitly assumes that most errors are well-balanced and/or negligibly small. In particular, the round-off error is often ignored based on the argument that it will be ‘sufficiently small’ if just IEEE-754 double-precision floating-point arithmetics [4] are adopted. In this paper, the focus is on the overall discretization error due to truncation and round-off. In particular, we will show that the latter might very well have a significant influence on the overall accuracy and propose a practical strategy to balance both error contributors.

The discretization error strongly depends on the number of degrees of freedom (“DoFs”), denoted by $N_h^{(p)}$, which is a function of the mesh width h and the approximation order p . The truncation error, denoted by E_T , dominates the discretization error only when $N_h^{(p)}$ is not too large, and it decreases with increasing mesh resolution and element degree as it can be expected from finite element theory [5]. Based on this, the commonly used approaches to reduce the truncation error are to reduce the mesh width (h -refinement), increase the approximation order (p -refinement), or apply both strategies simultaneously (hp -refinement) [6]. The round-off error, denoted by E_R , is, however, only negligible for moderately small values of $N_h^{(p)}$ and dominates the overall discretization error if more and more DoFs are employed [7]. Consequently, for a particular approximation order p , by performing h -refinement, the best accuracy is obtained at the break-even point where the discretization error is the smallest. We denote the highest accuracy by $E_{\min}^{(p)}$ and the optimal number of DoFs by $N_{\text{opt}}^{(p)}$.

While $N_{\text{opt}}^{(p)}$ is typically impractically large if low(est)-order approximations are used, it can be very small if high-order approximations are adopted, which are nowadays becoming more and more popular, and make the results more prone to be polluted by round-off errors. Despite this alarming observation, to the authors’ best knowledge, only very few publications address the impact of accumulated round-off errors on the overall accuracy of the final solution [8, 9] or take them into account explicitly in the error-estimation procedure [10, 11]. The general rule of thumb is still to perform as many h -refinements as possible considering the available computer hardware.

The aim of this paper is to systematically analyze the influence of the round-off error on the discretization error, for the solution, and its first and second derivative, and propose a practical approach for obtaining $E_{\min}^{(p)}$. The scope is restricted to one-dimensional model problems, i.e. Poisson, diffusion and Helmholtz equations, for which both the standard finite element method (FEM) and the mixed FEM[12] are considered. To assess the general applicability of the aforementioned approach, the following factors are investigated: the element degree over a wide range, first and second derivative of the solution, type of boundary conditions

and method of implementing them, choice and configuration of the linear system solver, order of magnitude
of the solution and its derivatives, and equation type.

The paper is organized as follows. The model problem, finite element formulation and numerical imple-
mentation are described in Section 2. The general behavior of the discretization error and the approach to
predict $E_{\min}^{(p)}$ are discussed in Section 3. Numerical results for determining the offset of the round-off error
are shown in Section 4. The algorithm for realizing the approach is put forward in Section 5, followed by
its validation by a Helmholtz problem in Section 6. The conclusions are drawn in Section 7.

2. Model problem, finite element formulation and numerical implementation

2.1. Model problem

Consider the following one-dimensional second-order differential equation:

$$(D(x)u_x)_x + r(x)u(x) = f(x), \quad x \in I = (0, 1), \quad (1)$$

with u denoting the unknown variable, which can either be real or complex, $f(x) \in L^2(I)$ a prescribed right-
hand side, and $D(x)$ and $r(x)$ continuous coefficient functions. By choosing $D(x) = 1$ and $r(x) = 0$, Eq. (1)
reduces to the Poisson equation; for $D(x) > 0$ and not constant, when $r(x) = 0$, the diffusion equation is
found, and when $r(x) \neq 0$, we obtain the Helmholtz equation. The boundary conditions are $u(x) = g(x)$ on
 Γ_D and $u_x = h(x)$ on Γ_N . Here, Γ_D and Γ_N are the boundaries where, respectively, Dirichlet and Neumann
boundary conditions are imposed. In this paper, for all the equations investigated, the existence of the
second derivative is guaranteed in the weak sense, i.e. $u \in H^2(I)$, see [12].

2.2. Finite element formulation

For convenience, we introduce the two inner products:

$$(f_1(x), f_2(x)) = \int_I f_1(x)f_2(x) dx, \quad (2a)$$

$$(g_1(x), g_2(x))_\Gamma = g_1(x_0)g_2(x_0), \quad (2b)$$

where $f_1(x)$, $f_2(x)$, $g_1(x)$ and $g_2(x)$ are continuous functions defined on the unit interval I , Γ denotes the
boundary of I , and x_0 denotes the value of x on Γ .

2.2.1. The standard FEM

The weak form of Eq. (1) is derived in Appendix A.1. Imposing the Dirichlet boundary conditions strongly, the weak form reads:

Weak form 1

Find $u \in H_D^1(I)$ such that:

$$-(\eta_x, Du_x) + (\eta, ru) = (\eta, f) - (\eta, Dhn)_{\Gamma_N} \quad \forall \eta \in H_{D0}^1(I),$$

with

$$H_D^1(I) = \{t \mid t \in H^1(I), t = g \text{ on } \Gamma_D\},$$

$$H_{D0}^1(I) = \{t \mid t \in H^1(I), t = 0 \text{ on } \Gamma_D\},$$

where n is 1 at $x = 1$, and -1 at $x = 0$.

(3)

By imposing the Dirichlet boundary conditions in the weak sense, the weak form reads:

Weak form 2

Find $u \in H^1(I)$ such that:

$$\begin{aligned} &-(\eta_x, Du_x) + (\eta, ru) + (\eta, Du_x n)_{\Gamma_D} - (\eta_x, un)_{\Gamma_D} + (\eta, \rho un)_{\Gamma_D} \\ &= (\eta, f) - (\eta, Dhn)_{\Gamma_N} - (\eta_x, gn)_{\Gamma_D} + (\eta, \rho gn)_{\Gamma_D} \quad \forall \eta \in H^1(I), \end{aligned}$$

where ρ is a positive value that serves as the penalty parameter.

(4)

Note that, the terms in the right-hand sides of Eqs. (3)–(4) consist of information of the Neumann boundary conditions, and hence, if no Neumann boundary conditions are prescribed, these terms vanish. We use Weak form 1 if not stated otherwise. Next, we approximate the exact solution u_{exc} by a linear combination of a finite number of basis functions:

$$u_{\text{exc}} \approx u_h^{(p)} = \sum_{i=1}^m u_i \varphi_i^{(p)}. \quad (5)$$

Here, $\varphi_i^{(p)}$ are C^0 -continuous Lagrange basis functions of degree p , denoted as P_p , with Gauss-Lobatto support points x_j , which feature the Kronecker-delta property, i.e. $\varphi_i^{(p)}(x_j) = \delta_{ij}$. The coefficients u_i are the values of $u_h^{(p)}$ at the DoFs, as a direct consequence of the Kronecker-delta property of $\varphi_i^{(p)}$. The number of DoFs of $u_h^{(p)}$, denoted by m , equals $p \times t + 1$, where t is the total number of the grid cells. Finally, taking the test function η equal to $\varphi_k^{(p)}$, $k = 1, 2, \dots, m$, we obtain

$$AU = F, \quad (6)$$

where A is the stiffness matrix, F the right-hand side and U the discrete solution, i.e. the vector of the coefficients u_i .

As a first step, we introduce the auxiliary variable

$$v(x) = -u_x, \quad (7a)$$

allowing Eq. (1) to be rewritten as

$$-D_x v(x) - D(x)v_x + r(x)u(x) = f(x). \quad (7b)$$

Unlike the standard FEM, for the mixed FEM, the essential boundary conditions are imposed on Γ_N , and the natural boundary conditions on Γ_D . The weak form of Eq. (1) using the mixed FEM, derived in Appendix A.2, is given by:

Weak form 3

Find $v \in H_N^1(I)$ and $u \in L^2(I)$ such that:

$$(w, v) - (w_x, u) = -(w, gn)_{\Gamma_D} \quad \forall w \in H_{N0}^1(I), \quad (8a)$$

$$-(q, D_x v) - (q, Dv_x) + (q, ru) = (q, f) \quad \forall q \in L^2(I), \quad (8b)$$

with

$$H_N^1(I) = \{t \mid t \in H^1(I), t = -h \text{ on } \Gamma_N\},$$

$$H_{N0}^1(I) = \{t \mid t \in H^1(I), t = 0 \text{ on } \Gamma_N\}.$$

Next, we approximate the exact gradient v_{exc} and the exact solution u_{exc} by a linear combination of a finite number of basis functions:

$$v_{\text{exc}} \approx v_h^{(p)} = \sum_{i=1}^n v_i \varphi_i^{(p)}, \quad (9a)$$

$$u_{\text{exc}} \approx u_h^{(p-1)} = \sum_{j=1}^p u_{cj} \psi_j^{(p-1)} \text{ in cell } c, \text{ for } c = 1, 2, \dots, t. \quad (9b)$$

where $\varphi_i^{(p)}$ are of the same type of basis functions used in Eq. (5), with coefficients v_i the associated values of $v_h^{(p)}$ at the DoFs; $\psi_j^{(p-1)}$ are discontinuous Lagrange basis functions of degree $p-1$, denoted as P_{p-1}^{disc} , with coefficients u_{cj} the associated values of $u_h^{(p-1)}$ at the DoFs. This pair of elements will be referred to as $P_p/P_{p-1}^{\text{disc}}$. Since the use of discontinuous basis functions, there are two independent $u_{c,j}$ at cell interfaces. The number of DoFs for $v_h^{(p)}$, denoted by n , equals $p \times t + 1$, and the number of DoFs for $u_h^{(p-1)}$ equals $p \times t$. Finally, replacing the test functions w and q by $\varphi_k^{(p)}$, $k = 1, 2, \dots, p \times t + 1$, and $\psi_e^{(p-1)}$, $e = 1, 2, \dots, p \times t$, respectively, the resulting coupled linear system of equations that has to be solved reads:

$$\begin{bmatrix} M & B \\ B^\top & 0 \end{bmatrix} \begin{bmatrix} V \\ U \end{bmatrix} = \begin{bmatrix} G \\ H \end{bmatrix}, \quad (10)$$

where the mass matrix M , the discrete gradient operator B , and its transpose, the discrete divergence operator B^\top , are the components of the discrete left-hand side of Eqs. (8a)–(8b), G and H are the components of the right-hand side, and V and U are the discrete first derivative and solution, i.e. the vectors of the coefficients v_i and u_{cj} , respectively.

For the sake of readability, we will drop the superscript (p) , whenever the approximation order is clear from the context.

2.3. Numerical implementation

In what follows, we demonstrate how to obtain the numerical solution for Eq. (1) with specific coefficients and assess its quality. For the latter, both the error, obtained using the analytical solution or the finer numerical solution, and the order of convergence are investigated.

2.3.1. Solution technique

Unless stated otherwise, all results are computed in IEEE-754 double precision [4] using the deal.II finite element code [13] that provides subroutines for creating the computational grid, building and solving the system of equations, and computing the error norms.

The computational mesh is obtained by globally refining a single element that covers the interval I , and the Dirichlet boundary conditions are imposed strongly unless stated otherwise. The former means that, when the solution is real valued, using the standard FEM, the number of DoFs equals $2^{REF} \times p + 1$ at the REF th refinement; using the mixed FEM, the number of DoFs equals $2 \times 2^{REF} \times p + 1$ at the REF th refinement. For complex-valued problems, the above numbers double since deal.II does not provide native support for complex-valued problems and, hence, all components need to be split into their real and imaginary parts.

To compute the occurring integrals, sufficiently accurate Gaussian quadrature formulas are used. Furthermore, unless stated otherwise, to solve the matrix equation, the UMFPACK solver [14], which implements the multi-frontal LU factorization approach, is used as it results in relatively fast computations of the problems considered in this paper, and prevents the iteration errors for the iterative solvers.

2.3.2. Error estimation

For the numerical results var_h , where var can be u , u_x and u_{xx} , the discretization error measured in the L_2 norm is used. This measure contains all types of errors, for example the truncation error, round-off error, etc. It is defined as

$$E_h = \|var_h - var_{\text{exc}}\|_2 \quad (11a)$$

when the exact solution var_{exc} is available, or [15]

$$\widetilde{E}_h = \|var_h - var_{h/2}\|_2 \quad (11b)$$

otherwise, where $var_{h/2}$ is the numerical solution computed on a mesh with grid size $h/2$. The derivatives, which are $u_{h,x}$ and $u_{h,xx}$ in the standard FEM and only $u_{h,xx}$ in the mixed FEM, are computed in the classical finite element manner, e.g. $u_{h,x}^{(p-1)} = \sum_{i=1}^m u_i \varphi_{i,x}^{(p)}$ yields an approximation to u_x using standard FEM.

110 Note that, each differentiation decreases the element degree by one.

2.3.3. Convergence of the solution

When the number of DoFs is relatively large, but the round-off error does not exceed the truncation error, the discretization error converges at a fixed rate β_T theoretically [5, Theorem 5.I]. The theoretical value of β_T is one order higher than the approximation order [5]. In practice, it can be calculated from either

$$Q = \log_2 \left(\frac{E_h}{E_{h/2}} \right) \quad (12a)$$

using Eq. (11a), or

$$\tilde{Q} = \log_2 \left(\frac{\widetilde{E_h}}{\widetilde{E_{h/2}}} \right) \quad (12b)$$

using Eq. (11b).

3. General behaviour of the discretization error and approach to predict the highest attainable accuracy

115 In this section, based on [7, 16], we illustrate the general behaviour of the discretization error E_h for Eq. (1) as a function of the number of DoFs N_h , and provide an approach to predict the highest attainable accuracy.

The discretization error of one variable for one p is illustrated in Fig. 1, where log-log axes are used.

120 As can be seen, the change of E_h with N_h can be divided into three phases according to N_c and N_{opt} , for which the former is N_h where E_h begins showing the expected asymptotic convergence behavior, and the latter is N_h where E_h begins increasing, i.e. where the highest attainable accuracy is obtained. The features of E_h in each phase are shown in Table 1.

As we will prove in section 4, the values of α_R and β_R can be relatively fixed. Therefore, the round-off error can be assessed before solving the problem. Moreover, since α_T can be inversed by using

$$\alpha_T = E_c / N_c^{-\beta_T}, \quad (13)$$

at the beginning of phase 2, where E_c is the value of E_h corresponding to N_c , we can forecast E_T afterwards.

Obviously, N_{opt} happens when $E_T + E_R$ is the smallest. By solving

$$\frac{d(E_T + E_R)}{dN} = 0, \quad (14)$$

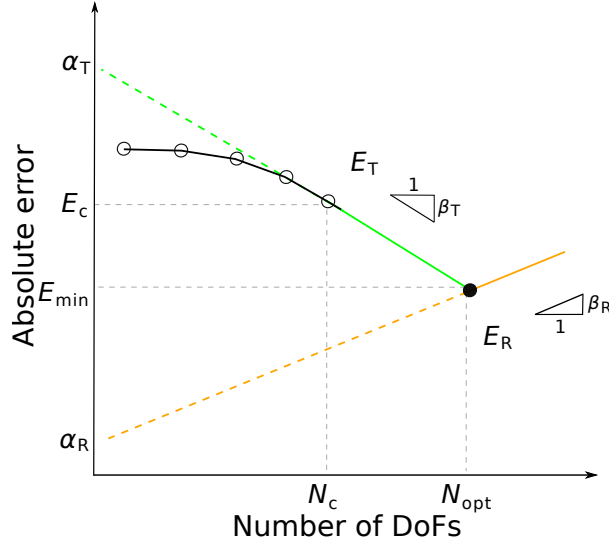


Fig. 1. Conceptual sketch of the dependency of the discretization error on the number of DoFs.

Table 1 Features of E_h in different phases.

	1. $N_h < N_c$	2. $N_c \leq N_h < N_{\text{opt}}$	3. $N_{\text{opt}} \leq N_h$
Description	Decreasing but not converging at slope β_T	Decreasing and converging at slope β_T , with the offset α_T	Increasing and converging at slope β_R , with the offset α_R
Formula	-	$E_h = \alpha_T N_h^{-\beta_T}$	$E_h = \alpha_R N_h^{\beta_R}$
Dominant error	Truncation error		Round-off error

we can predict

$$N_{\text{opt}} = \left(\frac{\alpha_T \beta_T}{\alpha_R \beta_R} \right)^{\frac{1}{\beta_T + \beta_R}}, \quad (15a)$$

and hence, the highest attainable accuracy

$$E_{\text{min}} = \alpha_T N_{\text{opt}}^{-\beta_T} + \alpha_R N_{\text{opt}}^{\beta_R}. \quad (15b)$$

4. Numerical quantification of the round-off error

125 In this section, we assess the general values for α_R and β_R for variables u , u_x and u_{xx} , using both the standard FEM and the mixed FEM. We start with the preliminary results obtained from three benchmark equations, and then investigate the following factors: solution strategies, orders of magnitude, coefficients $d(x)$ and $r(x)$, and boundary conditions.

Table 2 Settings of the benchmark Poisson, diffusion and Helmholtz equations.

	“Poisson”	“diffusion”	“Helmholtz”
$D(x)$	1	$1 + x$	$(1 + i)e^{-x}$
$r(x)$	0	0	$2e^{-x}$
$f(x)$	$e^{-(x-1/2)^2} (4x^2 - 4x - 1)$	$2\pi \cos(2\pi x) - 4\pi^2 \sin(2\pi x)(x + 1)$	0
$\ f(x)\ _2$	1.60	42.99	0.00
Boundary conditions	$u(0) = e^{-1/4}$	$u(0) = 0$	$u(0) = 1$
	$u(1) = e^{-1/4}$	$u_x(1) = 2\pi$	$u_x(1) = 0$
Analytical solution u_{exc}	$e^{-(x-1/2)^2}$	$\sin(2\pi x)$	$ae^{(1+i)x} + (1-a)e^{-ix}$, $a = 1/((1-i)e^{1+2i} + 1)$
$\ u_{\text{exc}}\ _2$	0.92	0.71	1.26

4.1. Preliminary results

130 We consider the benchmark equations given in Table 2, for which the L_2 norm of the analytical solution u_{exc} is of order 1. Element degrees p range from 1 to 5.

4.1.1. Benchmark Poisson equation

For the benchmark Poisson equation, the discretization error E_h for u , u_x and u_{xx} using both the standard FEM and the mixed FEM can be found in Fig. 2 and Fig. 3, respectively. The offset α_R and slope β_R are denoted in the figures, so are in the following figures of the same type.

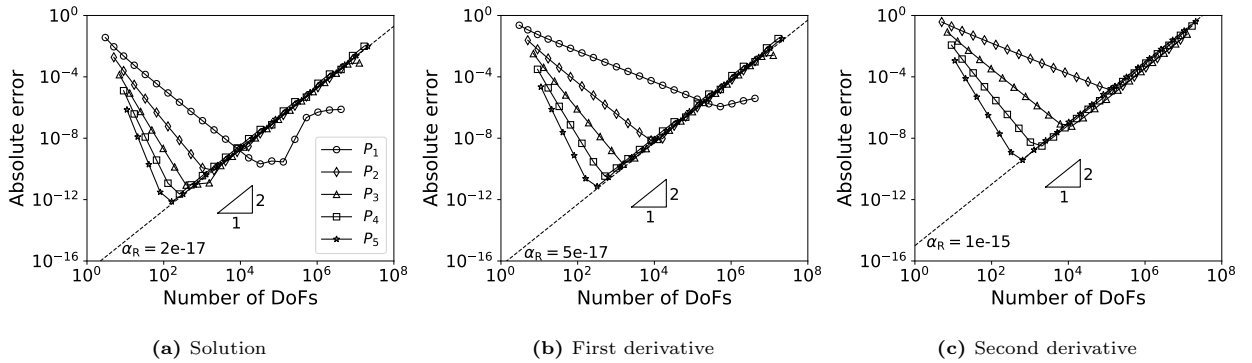


Fig. 2. Absolute errors for the benchmark Poisson equation using the standard FEM.

Using both the standard FEM and the mixed FEM, for all the variables, the interesting point is that the values of α_R and β_R for different element degrees tend to be the same. Notably, the value of the former is of order 10^{-16} , which is as expected when using double precision.

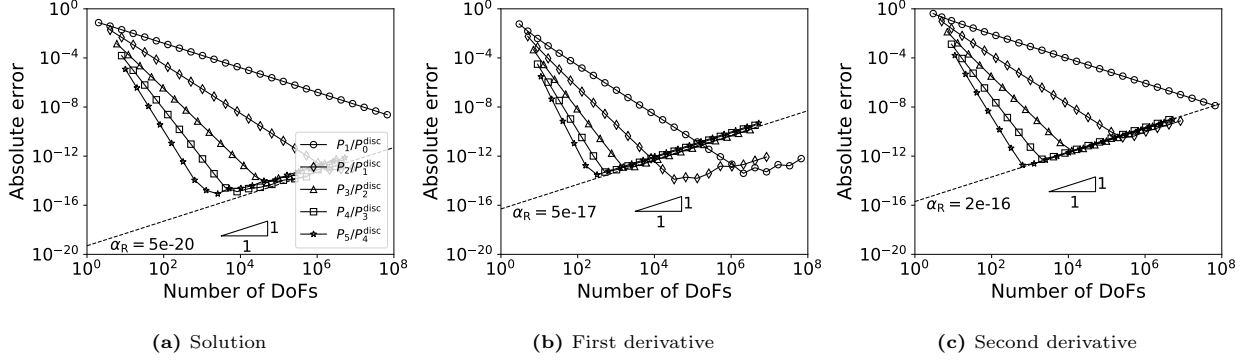


Fig. 3. Absolute errors for the benchmark Poisson equation using the mixed FEM.

For the error of one particular variable using one particular FEM, since E_T decreases faster for larger p , smaller E_{\min} can be obtained using larger p . Since the slope β_R using the mixed FEM is half of that using the standard FEM[17], the mixed FEM gives smaller E_{\min} for each variable using the same p , see Fig. 5(a) for the statistics.

It also shows that α_R tends to increase slightly with increasing order of derivative, see Fig. 4(a). Since E_T decreases slower after each differentiation, for the same element degree, using the standard FEM, E_{\min} tends to deteriorate with increasing order of derivative; using the mixed FEM, since the degree of the elements used for u_x is one order higher than that used for u , E_{\min} for u and u_x tend to be of the same order, but E_{\min} for u_{xx} is still larger than that for u_x , see Fig. 5(a) for the statistics.

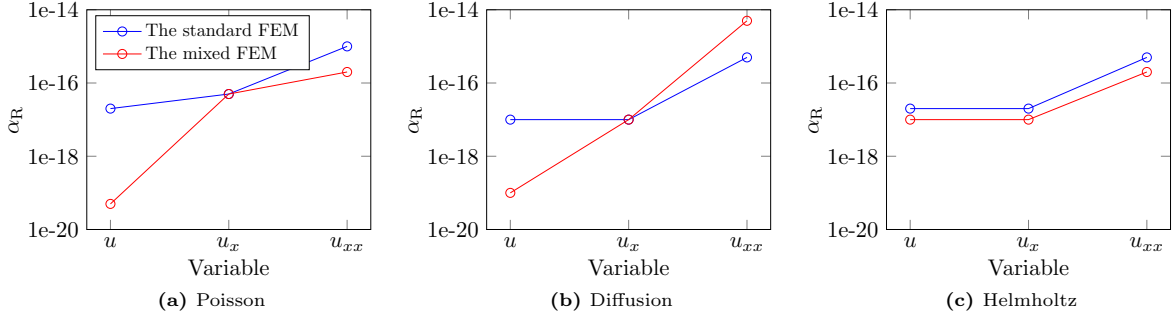


Fig. 4. α_R for the benchmark equations.

4.1.2. Benchmark diffusion and Helmholtz equations

For the benchmark diffusion and Helmholtz equations, the discretization errors are shown in Appendix B.1. The slopes β_R remain the same with that of the Poisson equation. The offsets α_R and E_{\min} also follow the same trend, see the rest of Fig. 4 and Fig. 5, respectively.

Summarizing this section, α_R varies not only with the variable, but also with the equation and FEM method; β_R is relatively fixed, which is 2 using the standard FEM and 1 using the mixed FEM. In what

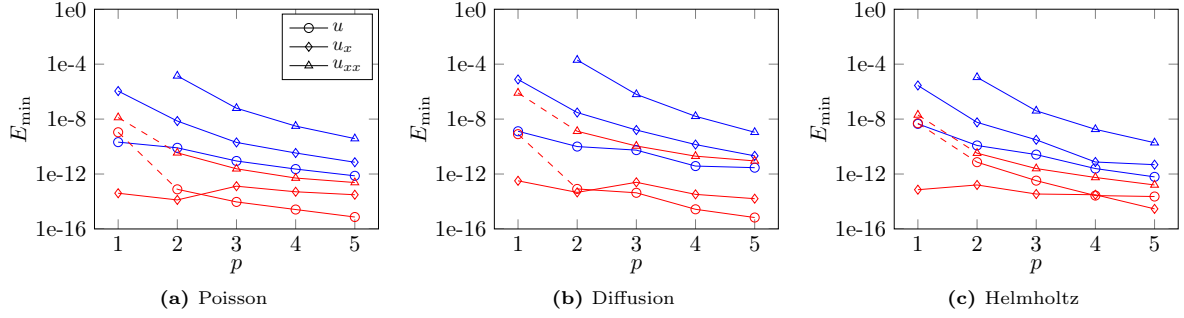


Fig. 5. E_{\min} for the benchmark equations. The blue color denotes the standard FEM, and the red color denotes the mixed FEM.

follows, we will take β_R as constant if not stated otherwise.

4.2. Sensitivity analysis

We focus on the benchmark Poisson equation, for which P_2 elements are used for the standard FEM, and P_4/P_3^{disc} elements are used for the mixed FEM.

4.2.1. Solution strategy

In this section, we investigate the influence of the solution strategy on the accuracy of the numerical solution. In particular, we compare the outcome when applying the direct solver UMFPACK with that of using the iterative Conjugate Gradient (CG) method [18], which can be applied since the system matrix A in Eq. (6) is symmetric and positive definite. The tolerance of the CG solver is set to be the product of a parameter, denoted by tol_{prm} , and the L_2 norm of the discrete right-hand side $\|F\|_2$. When the L_2 norm of the residual, i.e. $\|F - Au\|_2$ in Eq. (6), is smaller than the tolerance, the iteration is stopped. For the mixed FEM, we additionally investigate the impact of using a segregated solution approach based on the Schur complement instead of a fully coupled approach.

The standard FEM. The CG solver is stopped once $\|F - Au\|_2 \leq tol_{prm} \|F\|_2$, with $tol_{prm} = 10^{-10}$ and 10^{-4} , respectively. The absolute errors for u , u_x and u_{xx} using the CG solver are shown in Fig. 6, in comparison with that using the direct solver UMFPACK.

When tol_{prm} is adequately small, i.e. $tol_{prm} = 10^{-10}$, the round-off error for the solution and the first derivative using the CG solver is the same with that using the UMFPACK solver; the round-off error for the second derivative using the CG solver increases faster than that using the UMFPACK solver. When tol_{prm} is too large, i.e. $tol_{prm} = 10^{-4}$, the error contribution due to the iterative solver dominates both truncation and round-off errors.

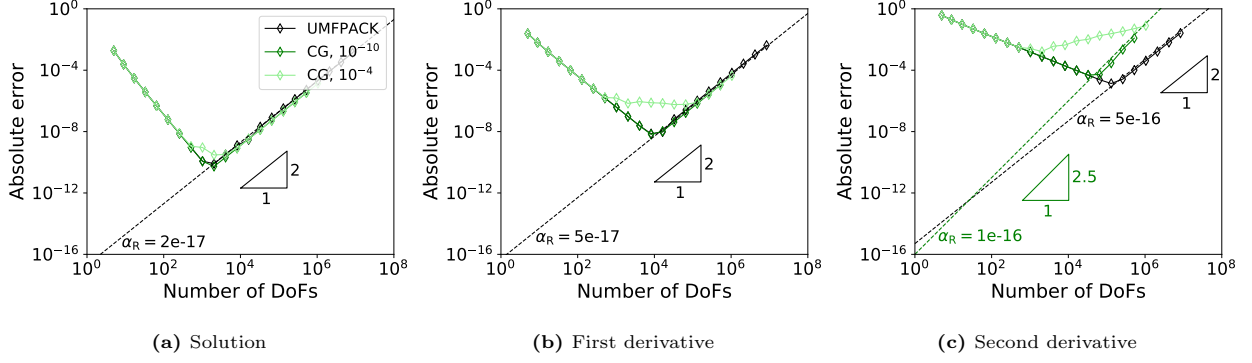


Fig. 6. Comparison of the errors using the CG solver and the UMFPACK solver.

The mixed FEM. Since the resulting matrix Eq. (10) is indefinite, a widely used alternative is to decouple the fully coupled monolithic approach

$$B^\top M^{-1}BU = B^\top M^{-1}G - H, \quad (16a)$$

$$MV = G - BU \quad (16b)$$

and solve both equations in segregated manner, i.e. Eq. (16a) is solved in the first place to obtain U , and then it is substituted into Eq. (16b) to obtain V .

Eq. (16a) involves the term $M^{-1}G$ in the right-hand side, which is computed by solving the auxiliary linear system $MY = G$ by using either the UMFPACK or the CG solver. The same options are available for solving Eq. (16b).

The difficulty in solving Eq. (16a) lies in not assembling the Schur complement matrix explicitly since it comprises M^{-1} . The CG solver only makes use of matrix-vector products of the form $(B^\top M^{-1}B)W$, which can be computed by the following three-step algorithm: $X = BW$, $MY = X$ and $Z = B^\top Y$. As before, the linear system $MY = X$ can be solved by the UMFPACK or the CG solver.

We first investigate the influence of tol_{prm} of the CG solver on the accuracy of the solutions when the left-hand side is $B^\top M^{-1}B$. In this case, the UMFPACK solver is used to solve the matrix equations when the left-hand side is M . For tol_{prm} being 10^{-16} and 10^{-10} , the results are shown in Fig. 7, in comparison with that obtained from solving the monolithic Eq. (10) directly using the UMFPACK solver. It shows that, for the problem at hand, the monolithic solution approach yields by far the most accurate solution and derivative values. Remarkably, the round-off error for v_x increases fastest using the Schur complement approach even though tol_{prm} is sufficiently small, i.e. $tol_{prm} = 10^{-16}$, which makes the highest attainable accuracy much lower. When tol_{prm} is less strict, i.e. $tol_{prm} = 10^{-10}$, the iteration error dominates the total error instead of the round-off error.

Next, we investigate the influence of tol_{prm} of the CG solver when the left-hand side is M . In this case, the CG solver with tol_{prm} being 10^{-16} is used to solve the matrix equation with the left-hand side being

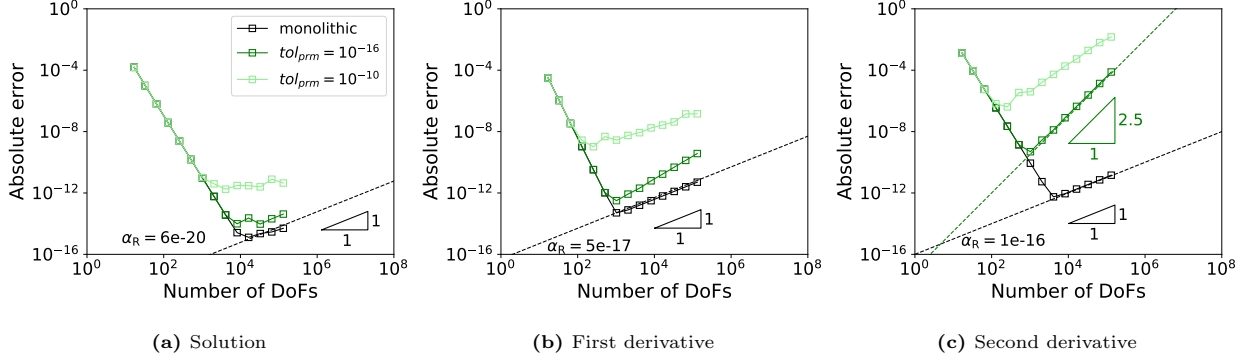


Fig. 7. Influence of the CG solver on the accuracy when the left-hand side is the Schur complement using the mixed FEM.

195 $B^\top M^{-1}B$. For tol_{prm} being 10^{-16} and 10^{-10} , the results are shown in Fig. 8, in comparison with that obtained from solving the monolithic Eq. (10) directly using the UMFPACK solver. It also shows that, when the tolerance is less strict, i.e. $tol_{prm} = 10^{-10}$, the iteration error dominates the total error before the round-off error.

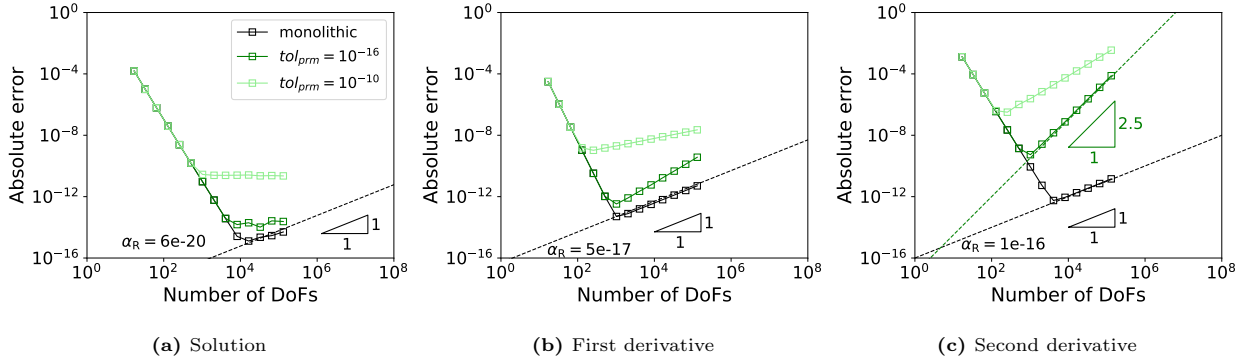


Fig. 8. Influence of the CG solver on the accuracy when the left-hand side is M using the mixed FEM.

In summary, for the standard FEM, the CG solver gives the same accuracy for u and u_x as the UMFPACK
 200 solver when tol_{prm} is strict enough, while the UMFPACK solver is recommended for computing u_{xx} ; for the mixed FEM, the accuracy for all the three variables is the highest when using the UMFPACK solver to solve the monolithic Eq. (10) directly. Moreover, the application of the CG solver on both the standard and mixed FEM methods shows that less strict values for tol_{prm} introduce iteration errors.

4.2.2. Order of magnitude

205 In this section, we investigate the influence of the order of magnitude of the solution and the right-hand side on the offset α_R of the round-off error and propose different scaling schemes to mitigate this influence factor. To cover a wide range of scenarios, we choose the right-hand sides shown in the second column of Table 3. The corresponding boundary conditions and analytical solutions are given in the remaining

columns of the table. Each case contains a coefficient c_i , $i = 1, 2, \dots, 5$, which is varied over several orders
of magnitude so that the L_2 norm of the exact solution, denoted by $\|u_{\text{exc}}\|_2$, and the L_2 norm of the
right-hand side, denoted by $\|f\|_2$, extend over a wide range of magnitudes. Fig. 9 gives an overview of
the distribution of $\|u_{\text{exc}}\|_2$ and $\|f\|_2$ for different cases, and the more detailed information can be found in
Fig. C.26.

Table 3 Setting of the Poisson equation with different right-hand sides.

Case	$f(x)$	Boundary conditions		$u_{\text{exc}}(x)$
		$u(0)$	$u(1)$	
1	$\sin(2\pi c_1 x)$	0	$(2\pi c_1)^{-2} \sin(2\pi c_1)$	$(2\pi c_1)^{-2} \sin(2\pi c_1 x)$
2	$-e^{-c_2(x-1/2)^2} \cdot (4c_2^2(x-1/2)^2 - 2c_2)$	$e^{-c_2/4}$	$e^{-c_2/4}$	$e^{-c_2(x-1/2)^2}$
3	$\sin(2\pi c_3 x) + 1$	0	$(2\pi c_3)^{-2} \sin(2\pi c_3) - \frac{1}{2}$	$(2\pi c_3)^{-2} \sin(2\pi c_3 x) - \frac{x^2}{2}$
4	$2\pi c_4 \sin(2\pi c_4 x)$	0	$(2\pi c_4)^{-1} \sin(2\pi c_4)$	$(2\pi c_4)^{-1} \sin(2\pi c_4 x)$
5	0	0	c_5^{-1}	$c_5^{-1} x$

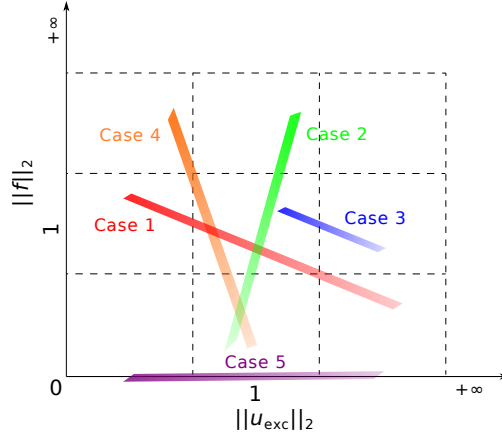


Fig. 9. Distribution of $\|u_{\text{exc}}\|_2$ and $\|f\|_2$ for the test cases with the settings from Table 3. The color density increases with the value of the coefficient c_i .

For case 1, the results are given below, and that of other cases can be found in Appendix C, which
shows qualitatively the same behavior.

The standard FEM. The absolute errors for u , u_x and u_{xx} for different values of c_1 using the standard FEM are depicted in Fig. 10. It shows that, for all the three variables, the offsets α_R increase with increasing $\|u\|_2$ (decreasing c_1), which makes it impossible to determine the break-even point between truncation and round-off error in a generic, that is, problem independent way.

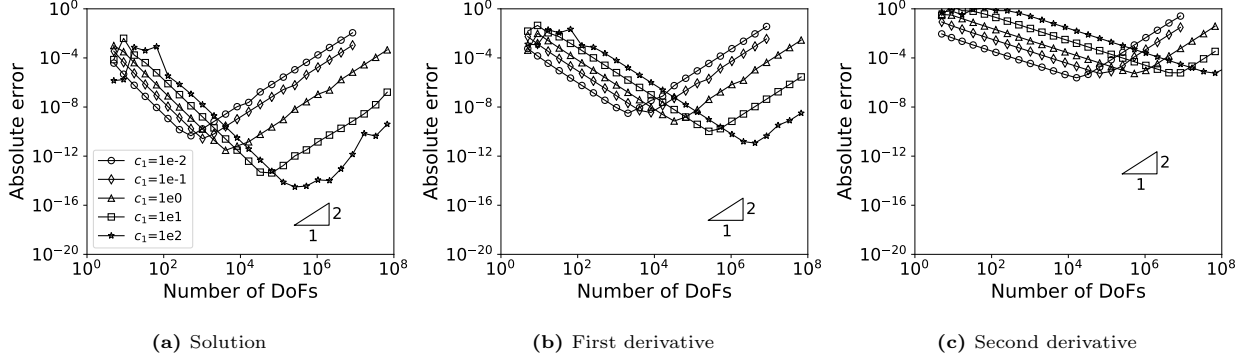


Fig. 10. Absolute errors for different c_1 using the standard FEM without scaling the right-hand side.

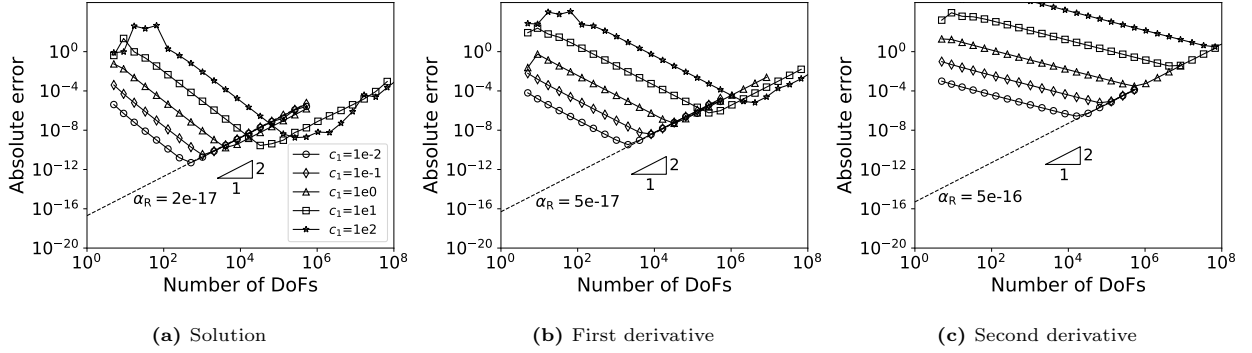


Fig. 11. Absolute errors for different c_1 using the standard FEM with scheme S .

This is because the number of accurate significant digits that the double-precision floating-point format can hold is 17 at most, and hence, more significant digits in the fractional part will be rounded with increasing $\|u\|_2$. To eliminate this influence factor, we scale the L_2 norm of u to 1, which is achieved by dividing the right-hand side F of the linear system of equations (6) by $\|u\|_2$. The scaling scheme can be found in the second row of Table 4, which is denoted as S . Note that, the scaling factor is approximated from the numerical solution through an a posteriori algorithm presented in Section 5.

Using scheme S for Case 1, the absolute errors are depicted in Fig. 11. It shows that α_R for different c_1 converge to common values, which are 2×10^{-17} , 5×10^{-17} and 5×10^{-16} for u , u_x and u_{xx} , respectively. These values also apply to Cases 2~5 when using scheme S .

The mixed FEM. The outcome of the numerical experiments performed with the mixed-FEM formulation Eq. (10) are presented in Fig. 12. Like with the standard FEM, the offsets α_R for u and u_x increase whenever $\|u\|_2$ and $\|u_x\|_2$ are increased.

Instinctively, to mitigate the influence of the magnitude of the solution u and the first derivative v on the offset α_R , one would scale the L_2 norm of u and v to 1. This can be achieved by dividing the right-hand sides G and H by the L_2 norm of the first derivative $\|v\|_2$ and multiplying the discrete first derivative operator B

Table 4 Scaling schemes.

Scheme	Left-hand side		Solution	Right-hand side
S	A		$\frac{1}{\ u\ _2}U$	$\frac{1}{\ u\ _2}F$
M_1	M	$\frac{\ u\ _2}{\ v\ _2}B$	$\frac{1}{\ v\ _2}V$	$\frac{1}{\ v\ _2}G$
	B^T	0	$\frac{1}{\ u\ _2}U$	$\frac{1}{\ v\ _2}H$
M_2	M	B	$\frac{1}{\ u\ _2}$	G
	B^T	0	V U	H

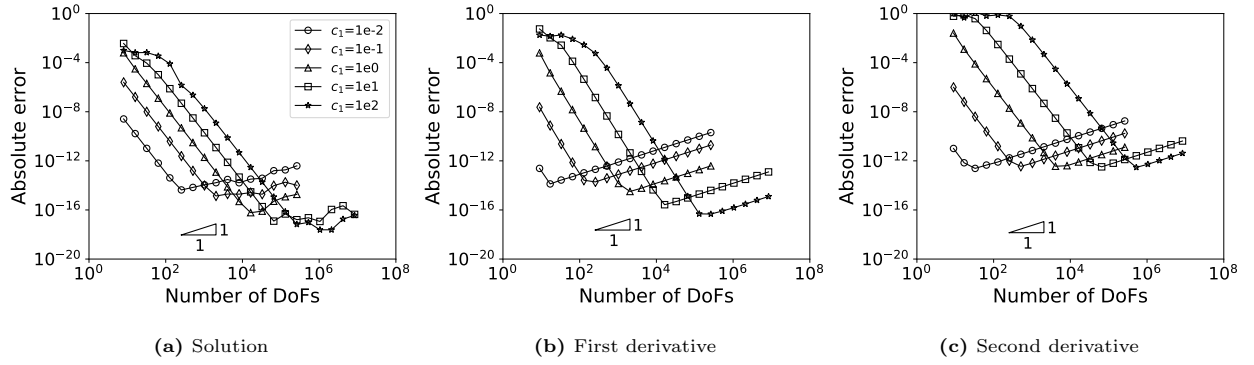


Fig. 12. Absolute errors for different c_1 using the mixed FEM without scaling the right-hand side.

235 by $\frac{\|u\|_2}{\|v\|_2}$, see scheme M_1 shown in Table 4. Using this scheme, the absolute errors of u , v and v_x are shown in Fig. 13. As expected, the offsets α_R for u and v_x converge, but that for v only converge when $c_1 < 1$. For $c_1 > 1$, no convergence of α_R is seen for v . It further indicates that we need smaller scaling factor for v when $c_1 > 1$.

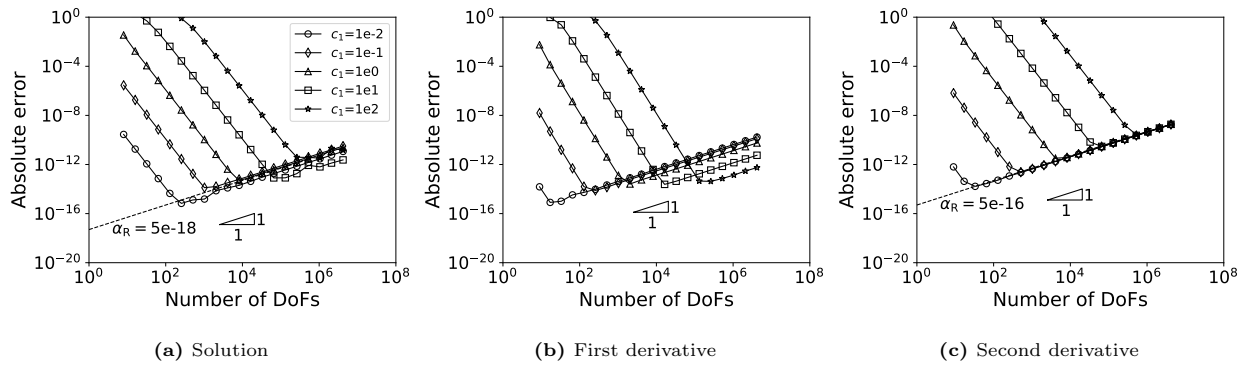


Fig. 13. Absolute errors for different c_1 using the mixed FEM with scheme M_1 .

Given that $\|u\|_2$ is of the same order with $\|v\|_2$ when $c_1 < 1$, while it is smaller than $\|v\|_2$ when $c_1 > 1$, we scale both u and v by $\|u\|_2$. This scaling scheme, which divides both the right-hand sides G and H by $\|u\|_2$, is denoted as scheme M_2 as shown in Table 4. The absolute errors obtained by using this scheme are shown in Fig. 14, where the offsets α_R for both u and v converge. However, not for v_x .

Therefore, scheme M_2 is preferable if u and v are of primary interest, and scheme M_1 is more suitable when v_x is of interest. If all three quantities need to be computed with required accuracy, both schemes M_1 and M_2 need to be applied side by side. The generalized values of α_R using the mixed FEM are 1×10^{-19} , 5×10^{-17} and 5×10^{-16} for u , v and v_x , respectively. These two scaling schemes also work for Cases 2~5, but the resulting α_R are slightly different. After being amended by Cases 2~5, α_R become 1×10^{-18} , 1×10^{-16} and 5×10^{-16} .

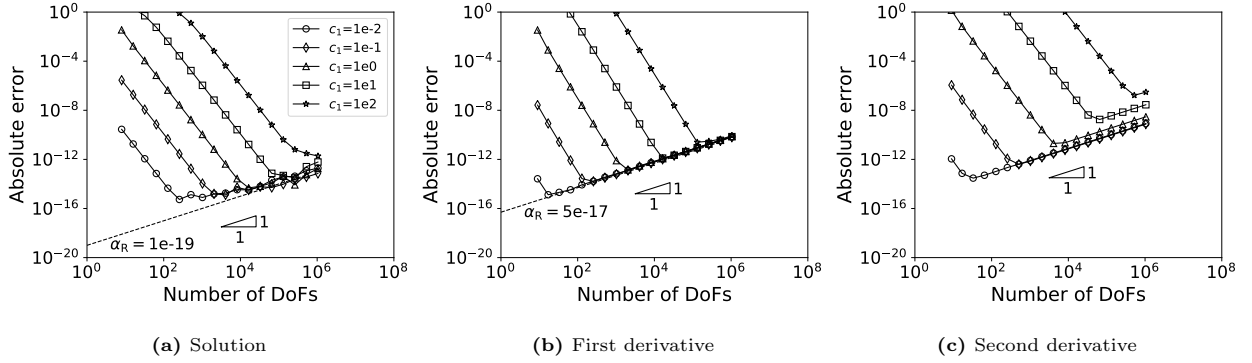


Fig. 14. Absolute errors for different c_1 using the mixed FEM with scheme M_2 .

Generalizing α_R using both the standard FEM and the mixed FEM for the Poisson equations, we obtain 2.0×10^{-17} , 5.0×10^{-17} and 5.0×10^{-16} for u , u_x and u_{xx} , respectively. Using the above scaling schemes for the benchmark diffusion and Helmholtz equations, we obtain values 2.0×10^{-17} , 2.0×10^{-17} and 1.0×10^{-15} . Generalizing these two sets of values, we obtain α_R shown in Table 5.

Table 5 Variable-independent α_R for Eq. (1) using both the standard and mixed FEMs.

	u	$u_x(v)$	$u_{xx}(v_x)$
α_R	2e-17	5e-17	1e-15

Summarizing this section, to mitigate the influence of the order of magnitude of the different variables on α_R , we have proposed and validated three different scaling schemes S , M_1 and M_2 , resulting in the common values for α_R . This is an essential prerequisite for our a posteriori refinement strategy to be robust and generally applicable.

4.2.3. $d(x)$ and $r(x)$

We consider the diffusion equations with $d(x)$ in Table 6 and the Helmholtz equations with $d(x)=1$ and $r(x)$ taken from the above constant $d(x)$, for which u is that of Case 2 with $c=1$ in Table 3.

Table 6 Various $d(x)$ for the diffusion equations.

Order	$d(x)$	$\ d\ _2$	Order	$d(x)$	$\ d\ _2$
1	0.01	0.01	7	$1 + \sin(10x)$	1.14
2	0.1	0.1	8	$1 + \sin(100x)$	1.06
3	1	1	9	$1 + x$	1.5
4	10	10	10	$1 + 10x$	6.7
5	100	100	11	$1 + 100x$	58.6
6	$1 + \sin(x)$	1.23			

For these two types of equations, the error basically evolves according to that shown in Fig. 1. To summarize, β_R is 2 using the standard FEM and 1 using the mixed FEM. α_R is shown in Figs. 15 and Fig. 16, respectively. In Fig. 15(b), the ratio is $2e-16$ and $5e-16$ for v and v_x , respectively. Therefore, we amend α_R for the mixed FEM to be that shown in Table 7.

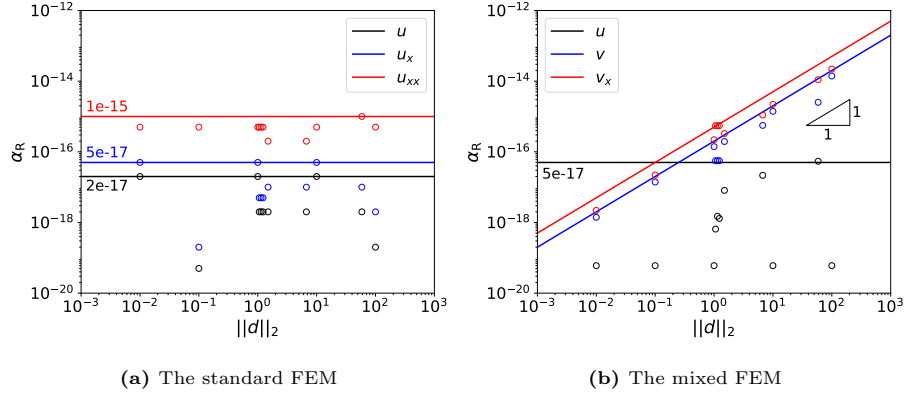


Fig. 15. α_R for the influence of $d(x)$.

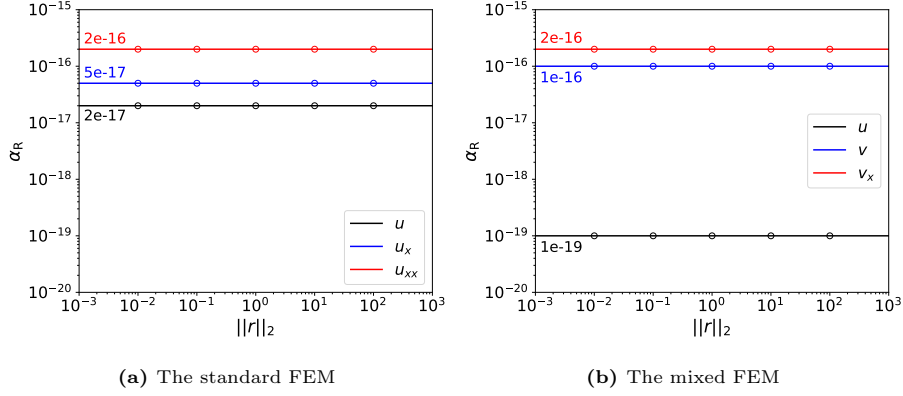


Fig. 16. α_R for the influence of $r(x)$.

Table 7 Variable-independent α_R for Eq. (1) after amendment.

(a) The standard FEM		(b) The mixed FEM	
u	2e-17	u	2e-17
u_x	5e-17	v	$2e-16 \times \ d\ _2$
u_{xx}	1e-15	v_x	1e-15

4.2.4. Boundary condition

In this section, two aspects of the influence of the boundary conditions on the round-off error are investigated: first the method of implementing the Dirichlet boundary conditions, and secondly types of boundary conditions.

For the first aspect, using Weak form 2 for $\rho = 50$ and 10^6 , the discretization errors are depicted in Fig. 17, in comparison with that using Weak form 1. As can be seen, both weak and strong imposition of the Dirichlet boundary condition yield the same trend line for the round-off error for the solution and its derivatives, and the magnitude of the penalty parameter in the weak imposition makes no difference. In addition, small penalty parameters might lead to larger truncation errors for u , but the difference diminishes when the penalty parameter is large enough.

To construct the problem for the second aspect, the Dirichlet boundary condition at the left boundary ($x = 0$) is kept while the Dirichlet boundary condition at the right boundary ($x = 1$) has been replaced by the Neumann boundary condition $u_x(1) = -e^{-1/4}$, leading to the same solution and derivative profiles.

The standard FEM. Using the standard FEM, the offsets α_R for the two types of boundary conditions are depicted in Fig. 18(a). For the Dirichlet/Neumann boundary condition, the offsets α_R for u and u_x are slightly larger than that for the Dirichlet/Dirichlet boundary condition by a factor of 3.5 and 2, respectively.

The offsets α_R for u_{xx} are identical for the two types of boundary conditions.

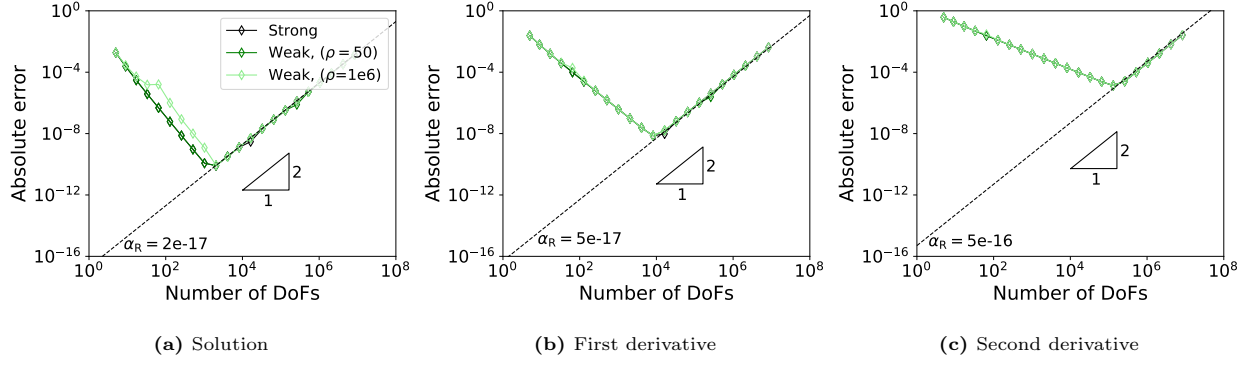


Fig. 17. Comparison of the errors for imposing the Dirichlet boundary condition strongly and weakly.

The mixed FEM. Using the mixed FEM, the offsets α_R for the two types of boundary conditions are depicted in Fig. 18(b). As can be seen, the type of boundary conditions plays a more important role for α_R for the solution than α_R for other variables.

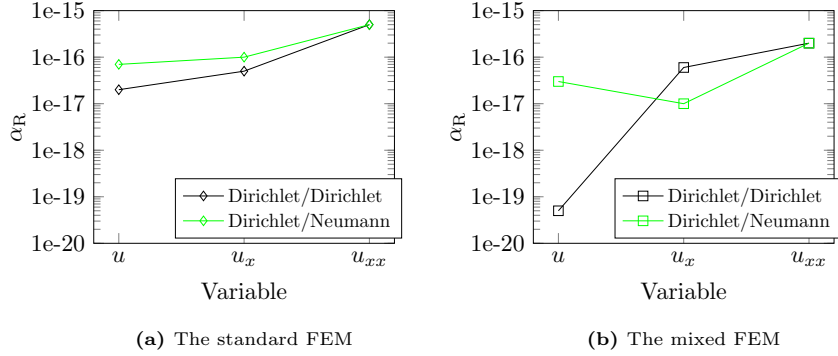


Fig. 18. Comparison of the errors for imposing Dirichlet/Dirichlet and Dirichlet/Neumann boundary conditions.

In summary, α_R are relatively independent of the variations in the type of boundary conditions and the method Dirichlet boundary conditions are implemented, which is an important prerequisite for our a posteriori refinement strategy to be applicable for a wide range of problems.

To conclude the sections on sensitivity analysis, the factors that cannot be mitigated are the tolerances for the iterative linear solver, that can be mitigated are the order of magnitude, and that are relatively irrelevant are the boundary conditions.

5. A posteriori algorithm for finding the optimal number of degrees of freedom

Based on the validation experiments from the previous section, we introduce a novel a posteriori algorithm for determining E_{\min} for the solution and its first and second derivative without performing the brute-force mesh refinement. Table 8 gives the default settings and the required custom input of the algorithm.

Table 8 Settings of the algorithm.

Item	Default	Custom
Problem	-	<ul style="list-style-type: none"> the differential equation to be solved its associated boundary conditions
Grid	<ul style="list-style-type: none"> initial number of vertices: 2 the vertices are equidistant 	-
FEM	<ul style="list-style-type: none"> the maximum N_h, denoted by N_{\max}, : 10^8 Dirichlet boundary conditions are imposed strongly 	<ul style="list-style-type: none"> standard or mixed formulation an ordered array of element degrees $\{p_{\min}, \dots, p_{\max}\}$
Computer precision	IEEE-754 double precision	-
Solver	UMFPACK	-
var	-	<ul style="list-style-type: none"> chosen from $\{u, u_x, u_{xx}\}$ error tolerance tol_{var}

Furthermore, we use the following coefficients in the algorithm:

- a minimal number of h -refinements before ‘*NORMALIZATION*’ and carrying out ‘*PREDICTION*’, denoted by REF_{\min} , with the following default values:

$$REF_{\min} = \begin{cases} 9 - p & \text{for } p < 6, \\ 4 & \text{otherwise.} \end{cases} \quad (17)$$

295 We choose this parameter mainly because the error might increase, or decrease faster than the theoretical order of convergence for coarse refinements, especially for lower-order elements.

- a stopping criterion c_s for seeking the scaling factor $\|var_{\text{exc}}\|_2$ in Table 4, its value is 0.001 by default. We choose this parameter because the analytical solution does not exist for most practical problems.
- a relaxation coefficient c_r for seeking the theoretical order of convergence, with the following default values:

$$c_r = \begin{cases} 0.9 & \text{for } p < 4, \\ 0.7 & \text{for } 4 \leq p < 10, \\ 0.5 & \text{otherwise.} \end{cases} \quad (18)$$

- the offset α_R , see Table 5 for the default values.

300 The procedure of our algorithm consists of four steps, which are explained below:

Step-1. ‘INPUT’. In this step, the custom input has to be provided.

Step-2. ‘NORMALIZATION’. The function of this step is to find the scaling factor to normalize problems of different orders of magnitude for the variable. The specific procedure can be found in Algorithm 1, where elements of degree p_{\min} are used.

Algorithm 1: NORMALIZATION

```

1 while  $N_h < N_{\max}$  do
2   if  $\left| \frac{\|var_h\|_2 - \|var_{2h}\|_2}{\|var_h\|_2} \right| < c_s$  then
3      $\|var_{\text{exc}}\|_2 \leftarrow \|var_h\|_2$ ;
4     break;
5   else
6      $h \leftarrow h/2$ ;
7     calculate  $\|var_h\|_2$  using Eq. (11a) without scaling;
8   end
9 end

```

Step-3. ‘PREDICTION’. This step finds E_{\min} for each var and p of interest, as illustrated in Fig. 1. The procedure for carrying out this step can be found in Algorithm 2.

Algorithm 2: PREDICTION

```

1 while  $\widetilde{E}_h > E_R$  and  $N_h < N_{\max}$  do
2    $\widetilde{Q} \leftarrow \log_2 (\widetilde{E}_{2h}/\widetilde{E}_h)$ ;
3   if  $\widetilde{Q} \geq \beta_T \times c_r$  then
4      $N_c \leftarrow N_h$ ;
5      $E_c \leftarrow \widetilde{E}_h$ ;
6      $\alpha_T \leftarrow E_c/N_c^{-\beta_T}$ ;
7      $N_{\text{opt}} \leftarrow \left( \frac{\alpha_T \beta_T}{\alpha_R \beta_R} \right)^{\frac{1}{\beta_R + \beta_T}}$ ;
8      $E_{\min} \leftarrow \alpha_T N_{\text{opt}}^{-\beta_T} + \alpha_R N_{\text{opt}}^{\beta_R}$ ;
9   else
10     $h \leftarrow h/2$ ;
11    calculate  $\widetilde{E}_h$  using Eq. (11b) with proper scaling schemes;
12  end
13 end

```

Step-4. ‘OUTPUT’. In this step, we output E_{\min} obtained from *Step-3*.

310 6. Validation

In what follows, we validate the strategy discussed in Section 3 by using the following Helmholtz problem:

$$((0.01 + x)(1.01 - x)u_x)_x - (0.01i)u(x) = 1.0, \quad x \in I = (0, 1), \quad (19)$$

with homogeneous Dirichlet and Neumann boundary conditions imposed as follows: $u(0) = 0$ and $u_x(1) = 0$.

Both the standard FEM and the mixed FEM are investigated, and the element degree p has a range of $\{1, 2, \dots, 5\}$. Variables u , u_x and u_{xx} are all investigated, for which tol_{var} is set to be 10^{-9} .

Using the prediction approach and the brute-force approach, E_{\min} are compared in Fig. 19. As can be seen, E_{\min} can be predicted correctly.

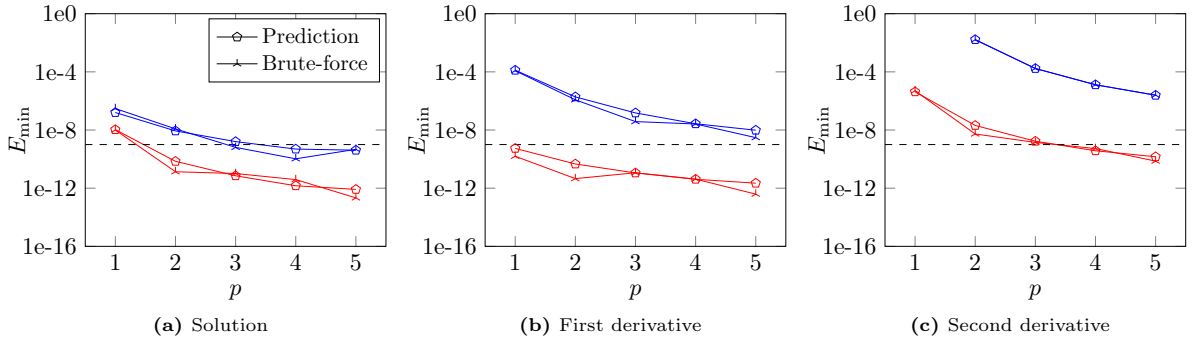


Fig. 19. Comparison of E_{\min} for Eq. (19) using the algorithm and the brute-force refinement. The blue color denotes the standard FEM, and the red color denotes the mixed FEM.

The CPU time required by the prediction approach (PRED) and the brute-force approach (BF) is shown in Fig. 20. Next to time PRED, and the computation time for the optimal grid (PRED+) using the prediction approach is also given. As can be seen, both time BF and time PRED+ decrease with increasing element degree. Time PRED+ is much smaller compared to time BF, see Fig. 21 for the percentage of the CPU time saved by PRED+, which shows a saving of the CPU time basically more than 60% and 40% for the standard FEM and the mixed FEM, respectively. Last but not least, time PRED is negligible compared to time PRED+.

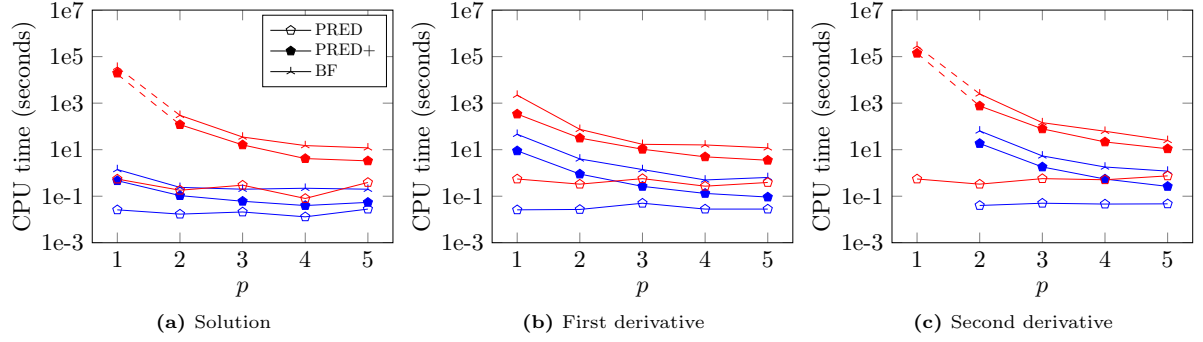


Fig. 20. Comparison of the CPU time to obtain E_{\min} for Eq. (19) using the algorithm and the brute-force refinement. The blue color denotes the standard FEM, and the red color denotes the mixed FEM.

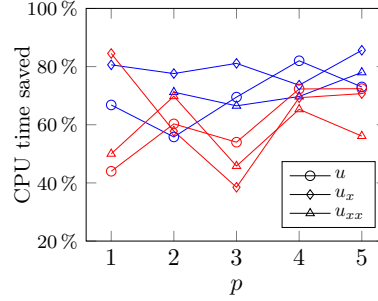


Fig. 21. Percentage of CPU time saved using the algorithm. The blue color denotes the standard FEM, and the red color denotes the mixed FEM.

Furthermore, the dashed line indicating the desired error tolerance in Fig. 19 cannot be reached using the standard FEM, whereas it can be reached using the mixed FEM with P_4/P_3^{disc} or better. When using P_4/P_3^{disc} , N_{opt} for u , u_x and u_{xx} are predicted to be 6042, 9812 and 123486, respectively.

7. Conclusions

A novel approach is presented to predict the highest attainable accuracy for second-order ordinary differential equations using the finite element methods. In contrast to the brute-force approach, which uses successive h -refinements, this approach uses only a few coarse grid refinements. This approach is viable for the solution and its first and second derivative, for both the standard FEM and the mixed FEM, and different element degrees. The algorithm for implementing the approach shows that the highest attainable accuracy can be accurately predicted and the CPU time is significantly reduced. To compute the solution of the highest attainable accuracy using our approach, the CPU time can be saved more than 60% for the standard FEM and 40% for the mixed FEM.

Future research will focus on the validation of the approach for 2D second-order problems, where the influence of the linear system solver, local mesh refinement and boundary conditions might be significantly

different from 1D problems.

Appendix A. Derivation of the weak form

Appendix A.1. The standard FEM

Multiply Eq. (1) by a test function $\eta \in H^1(I)$, and integrate it over I yields

$$(\eta, (Du_x)_x + ru) = (\eta, f). \quad (\text{A.1})$$

By applying Gauss's theorem for the first term of the left-hand side of Eq. (A.1), we obtain

$$-(\eta_x, Du_x) + (\eta, ru) = (\eta, f) - (\eta, Du_x n)_{\Gamma_N}. \quad (\text{A.2})$$

Therefore, without considering the boundary conditions, the weak form reads

Find $u \in H^1(I)$ such that:

$$-(\eta_x, Du_x) + (\eta, ru) = (\eta, f) - (\eta, Du_x n)_{\Gamma_N} \quad \forall \eta \in H^1(I),$$

where n is 1 at $x = 1$, and -1 at $x = 0$.

(A.3)

340 Imposing the original Dirichlet boundary conditions on u and the corresponding homogeneous Dirichlet boundary conditions on η in Eq. (A.3), which is called the strong imposition of the Dirichlet boundary conditions, the weak form can be found in Eq. (3). Instead of imposing the Dirichlet boundary conditions directly on the variables u and η in Eq. (A.3), by adding auxiliary terms [19], which is called the weak imposition of the Dirichlet boundary conditions, we obtain the weak form Eq. (4).

345 Appendix A.2. The mixed FEM

To obtain the weak form of Eq. (7), Eq. (7a) is multiplied by a test function of v , i.e. $w \in H_{N0}^1(I)$, and integrated over I , yielding

$$(v + u_x, w) = 0, \quad (\text{A.4a})$$

and Eq. (7b) is multiplied by a test function of u , i.e. $q \in L^2(I)$, and integrated over I , yielding

$$-(q, D_x v) - (q, Dv_x) + (q, ru) = (q, f). \quad (\text{A.4b})$$

By applying Gauss's theorem to Eq. (A.4a) and imposing the natural boundary condition $u(x) = g(x)$ on Γ_D , we obtain

$$(w, v) - (w_x, u) = -(w, gn)_{\Gamma_D}. \quad (\text{A.4c})$$

The resulting weak form can be found in Eq. (8).

Appendix B. Numerical results of the benchmark diffusion and Helmholtz equations

Appendix B.1. The diffusion equation

For the benchmark diffusion equation, using both the standard FEM and the mixed FEM, the absolute errors for all *three* variables are shown in Fig. B.22 and Fig. B.23, respectively.

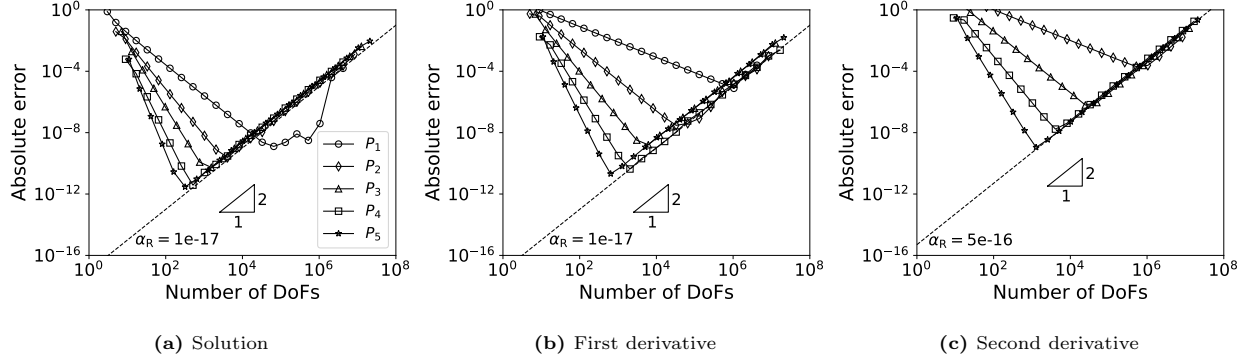


Fig. B.22. Absolute errors for the benchmark diffusion equation using the standard FEM.

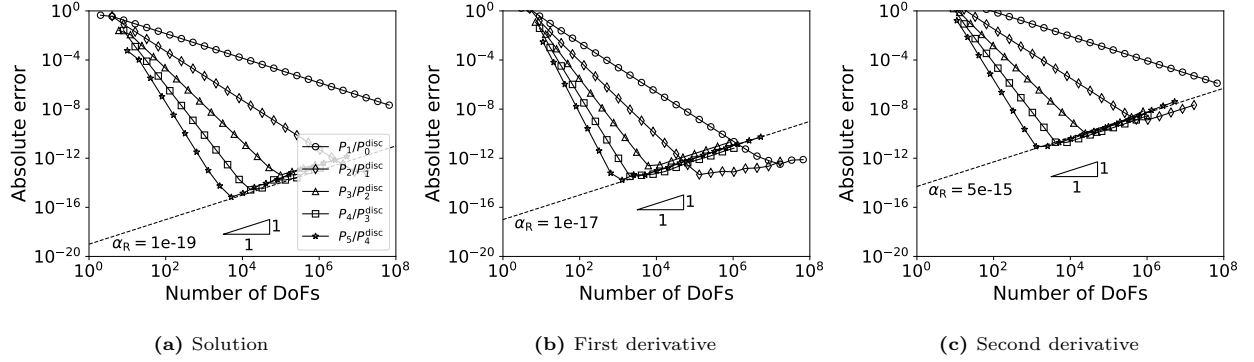


Fig. B.23. Absolute errors for the benchmark diffusion equation using the mixed FEM

Appendix B.2. The Helmholtz equation

For the benchmark Helmholtz equation, using both the standard FEM and the mixed FEM, the absolute errors for all *three* variables are shown in Fig. B.24 and Fig. B.25, respectively.

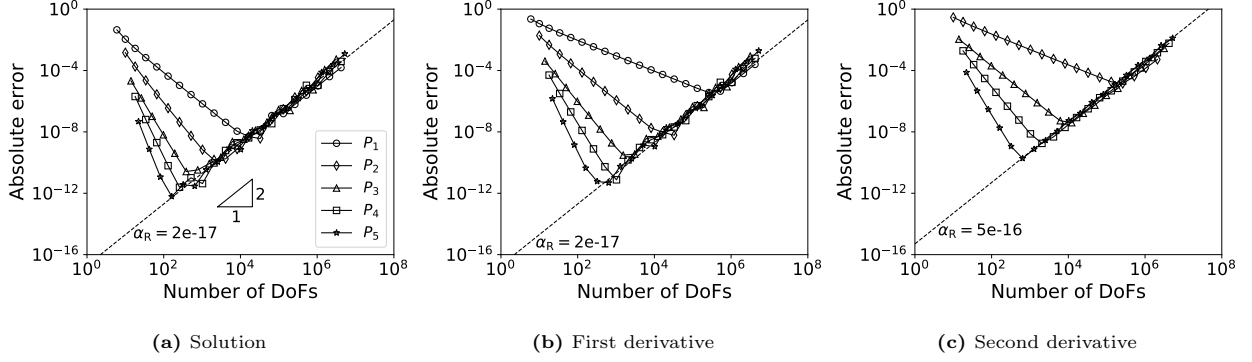


Fig. B.24. Absolute errors for the benchmark Helmholtz equation using the standard FEM.

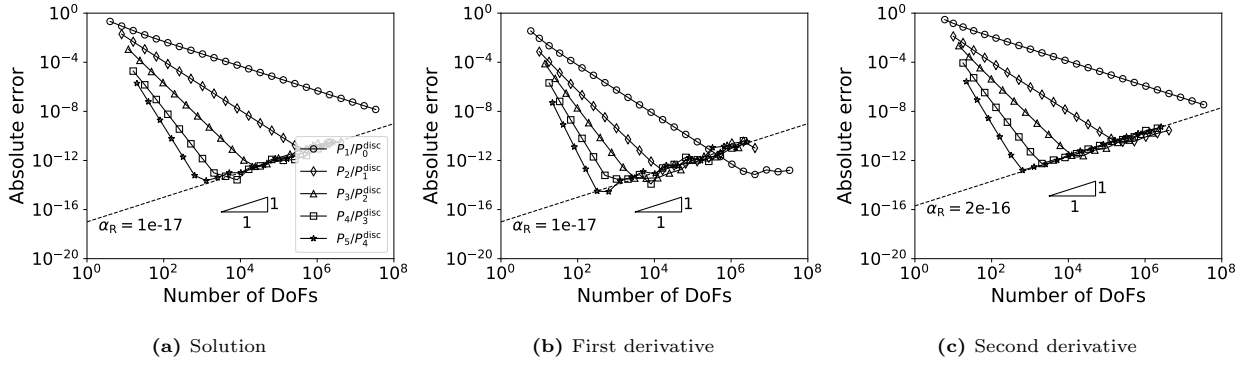


Fig. B.25. Absolute errors for the benchmark Helmholtz equation using the mixed FEM.

Appendix C. L_2 norms and absolute errors for different cases in Table 3

355 Appendix C.1. L_2 norms

The L_2 norms of u , u_x and/or $u_{xx}(f)$ for different cases are shown in Fig. C.26.

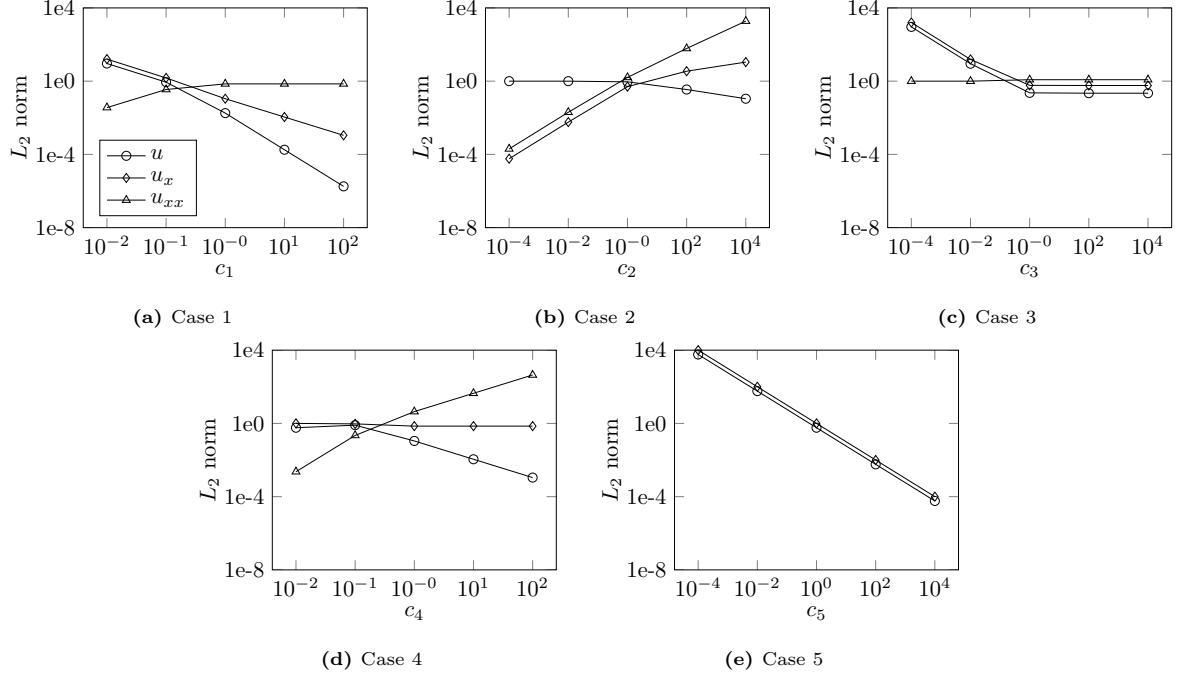


Fig. C.26. L_2 norms of u , u_x and u_{xx} for different cases in Table 3.

Appendix C.2. Absolute errors

Appendix C.2.1. The standard FEM

Case 2. For Case 2, using the standard FEM without scaling the right-hand side and scheme S, the absolute errors are shown in Figs. C.27–C.28.

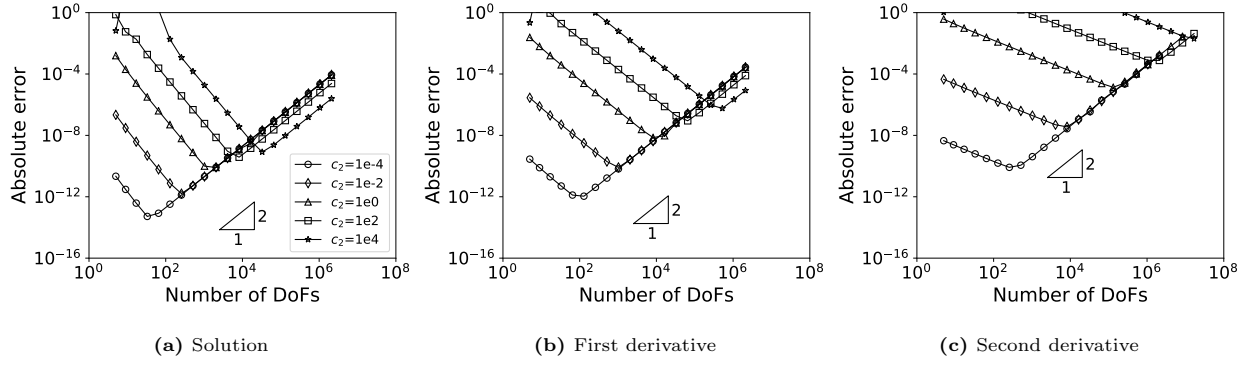


Fig. C.27. Absolute errors for Case 2 in Table 3 using the standard FEM without scaling the right-hand side.

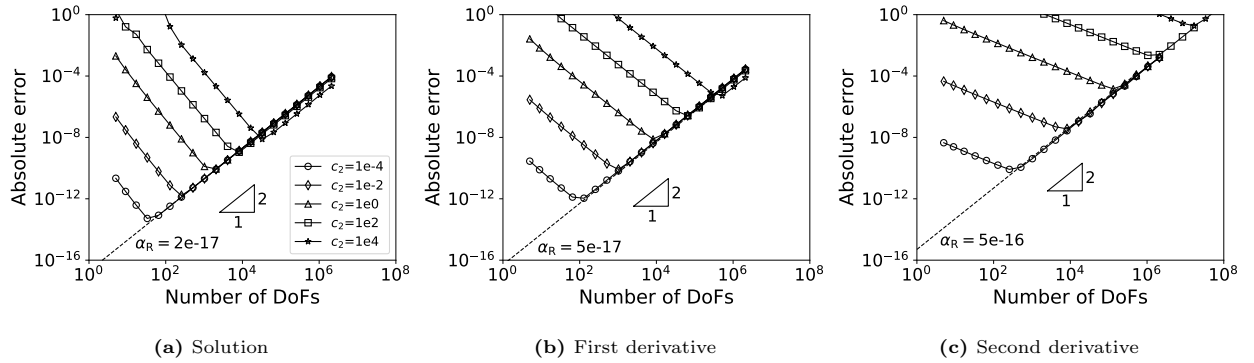


Fig. C.28. Absolute errors for Case 2 in Table 3 using scheme S.

Case 3. For Case 3, using the standard FEM without scaling the right-hand side and scheme S, the absolute errors are shown in Figs. C.29–C.30.

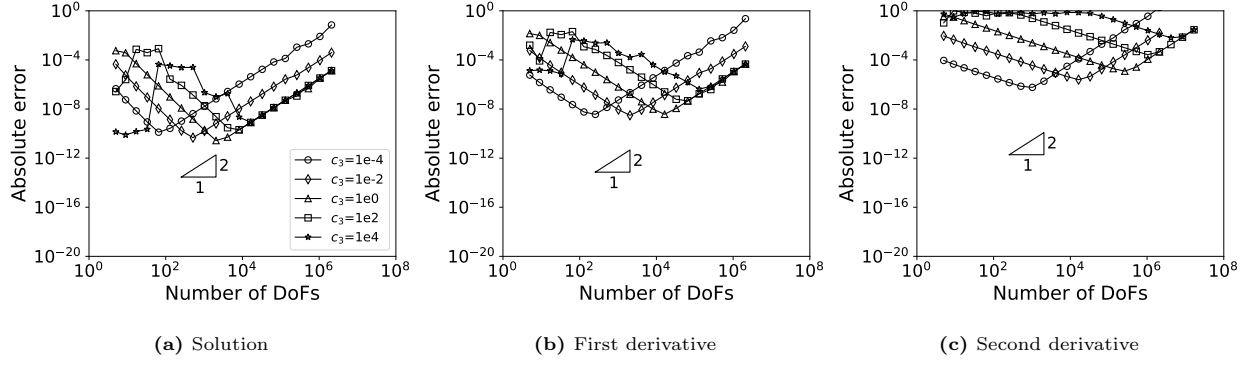


Fig. C.29. Absolute errors for Case 3 in Table 3 using the standard FEM without scaling the right-hand side.

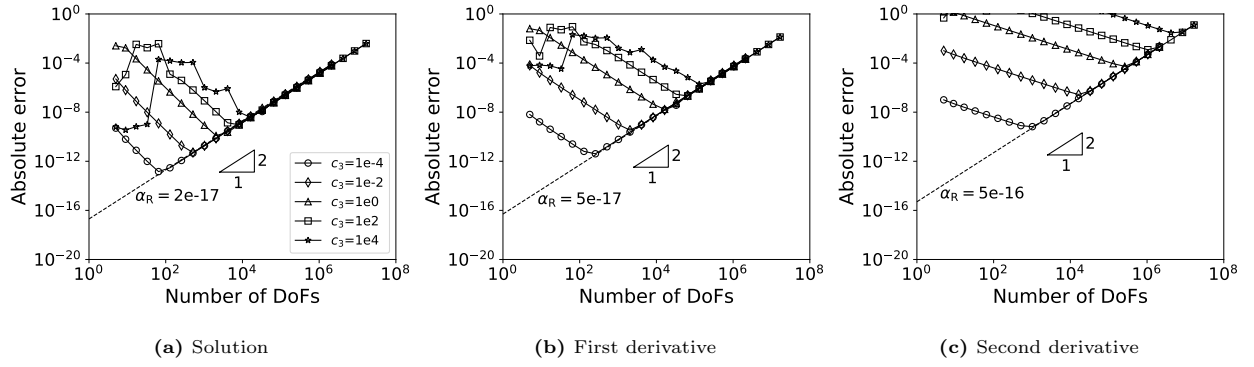


Fig. C.30. Absolute errors of Case 3 in Table 3 using scheme S .

Case 4. For Case 4, using the standard FEM without scaling the right-hand side and scheme S , the absolute errors are shown in Figs. C.31–C.32.

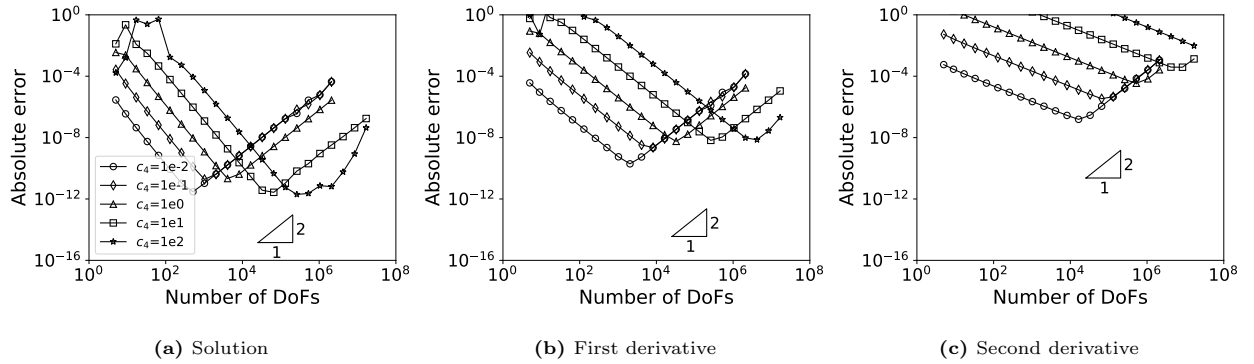


Fig. C.31. Absolute errors for Case 4 in Table 3 using the standard FEM without scaling the right-hand side.

Case 5. For Case 5, using the standard FEM without scaling the right-hand side and scheme S , the absolute errors are shown in Figs. C.33–C.34.

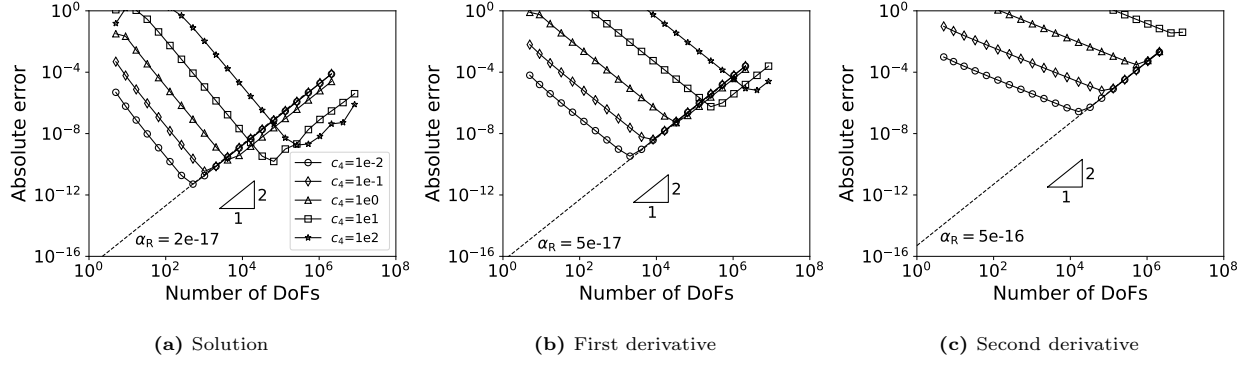


Fig. C.32. Absolute errors of Case 4 in Table 3 using scheme S .

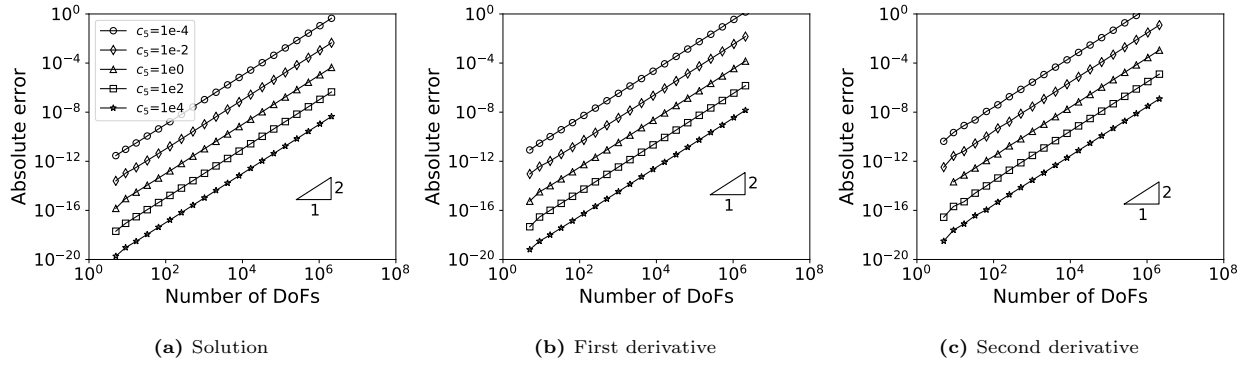


Fig. C.33. Absolute errors for Case 5 in Table 3 using the standard FEM without scaling the right-hand side.

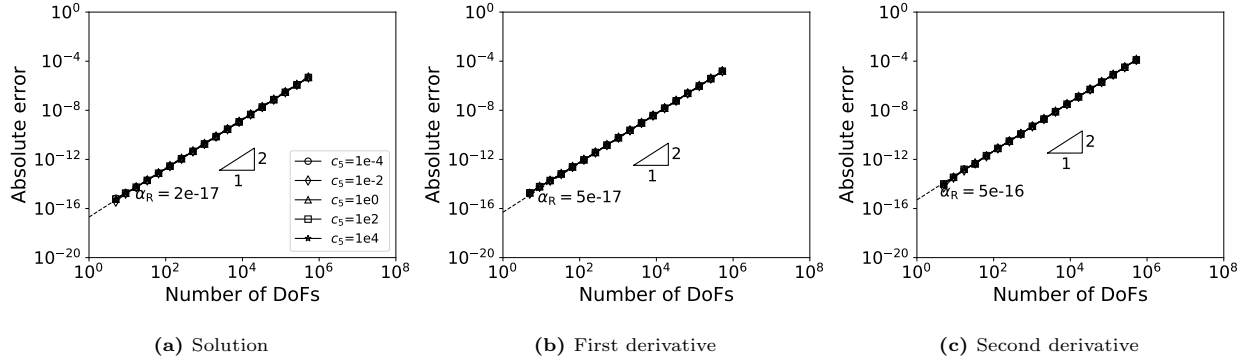


Fig. C.34. Absolute errors of Case 5 in Table 3 using scheme S .

Appendix C.2.2. The mixed FEM

Case 2. For Case 2, using the mixed FEM without scaling the right-hand side and schemes M_1 and M_2 , the absolute errors are shown in Figs. C.35–C.37.

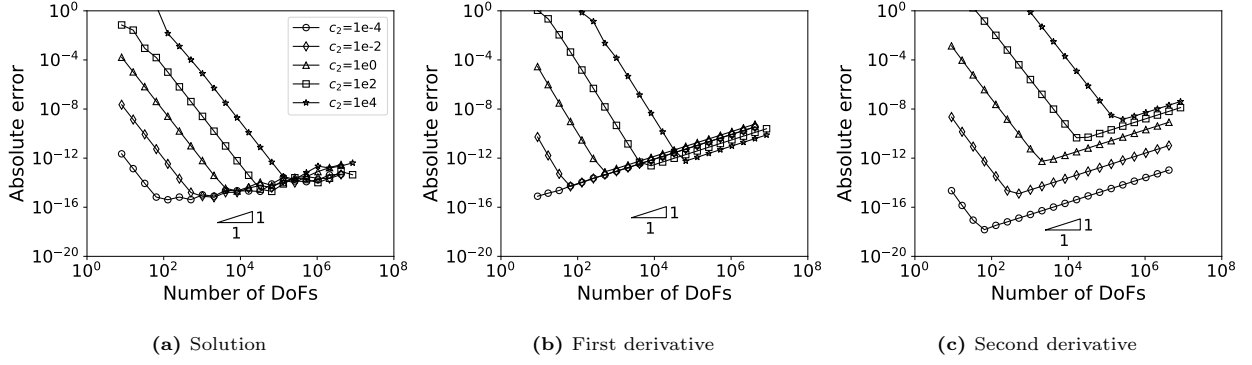


Fig. C.35. Absolute errors for Case 2 in Table 3 using the mixed FEM without scaling the right-hand side.

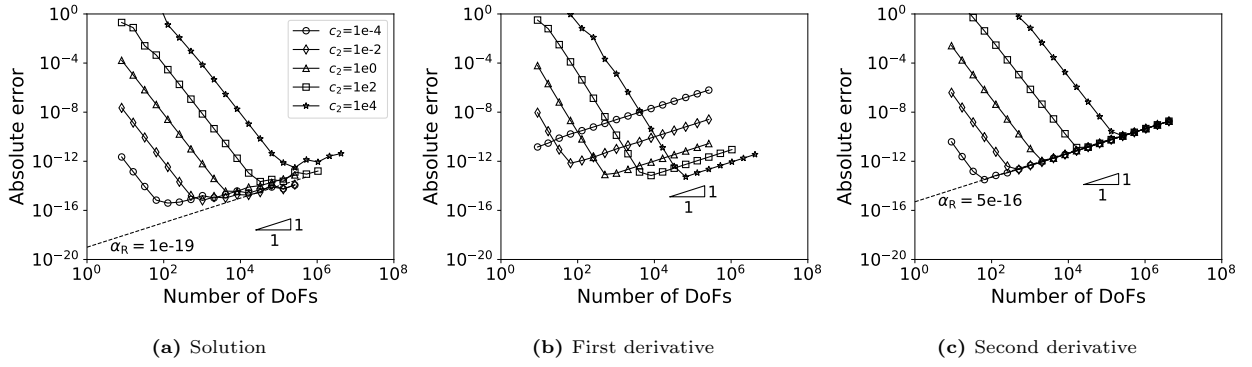


Fig. C.36. Absolute errors for Case 2 in Table 3 using scheme M_1 .

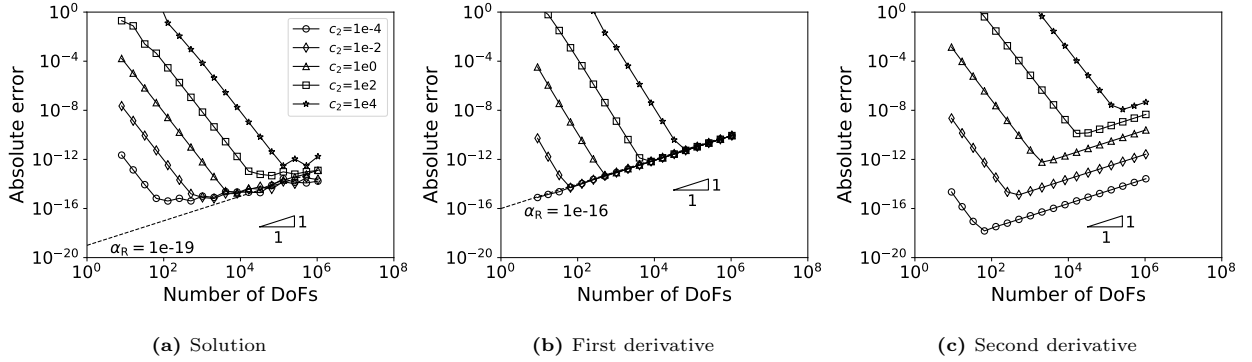


Fig. C.37. Absolute errors for Case 2 in Table 3 using scheme M_2 .

370 *Case 3.* For Case 3, using the mixed FEM without scaling the right-hand side and schemes M_1 and M_2 , the absolute errors are shown in Figs. C.38–C.40.

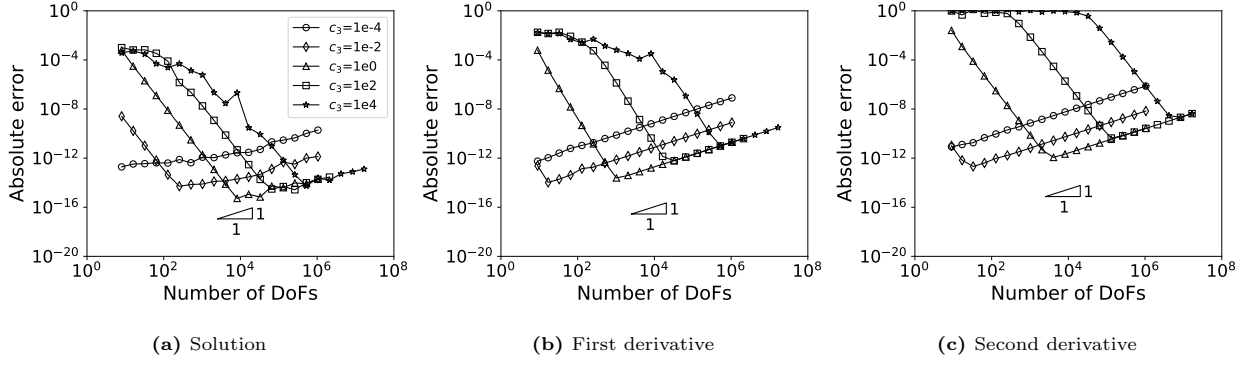


Fig. C.38. Absolute errors for Case 3 in Table 3 using the mixed FEM without scaling the right-hand side.

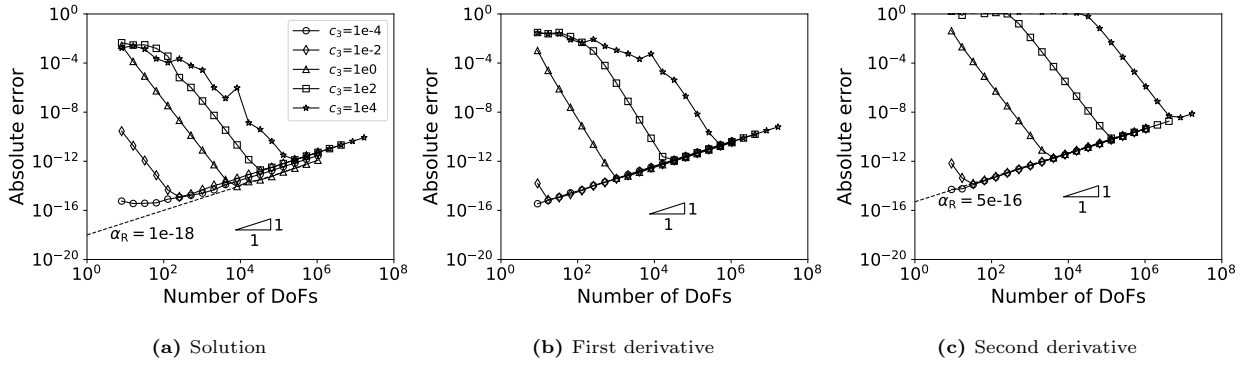


Fig. C.39. Absolute errors for Case 3 in Table 3 using scheme M_1 .

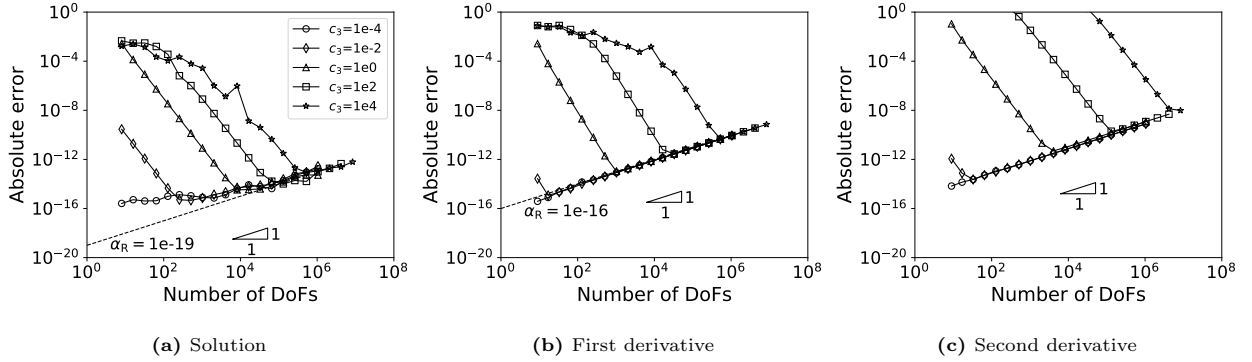


Fig. C.40. Absolute errors for Case 3 in Table 3 using scheme M_2 .

Case 4. For Case 4, using the mixed FEM without scaling the right-hand side and schemes M_1 and M_2 , the absolute errors are shown in Figs. C.41–C.43.

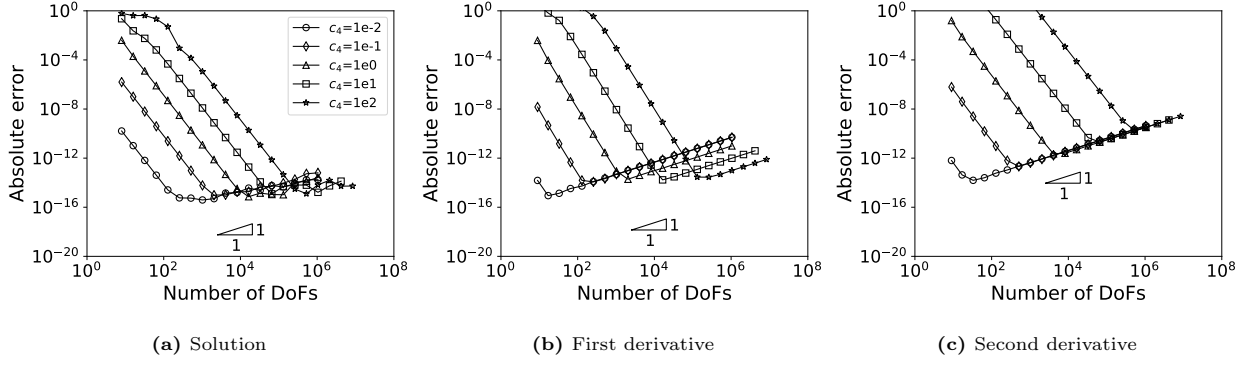


Fig. C.41. Absolute errors for Case 4 in Table 3 using the mixed FEM without scaling the right-hand side.

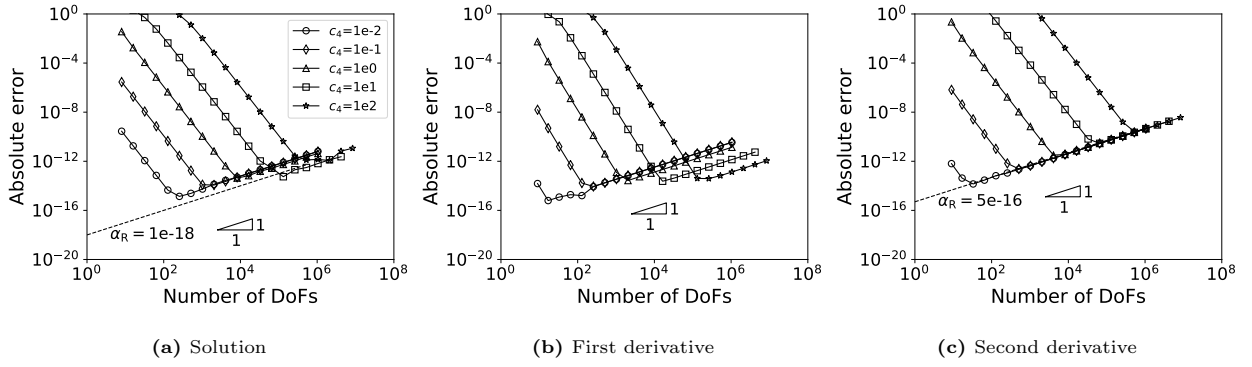


Fig. C.42. Absolute errors for Case 4 in Table 3 using scheme M_1 .

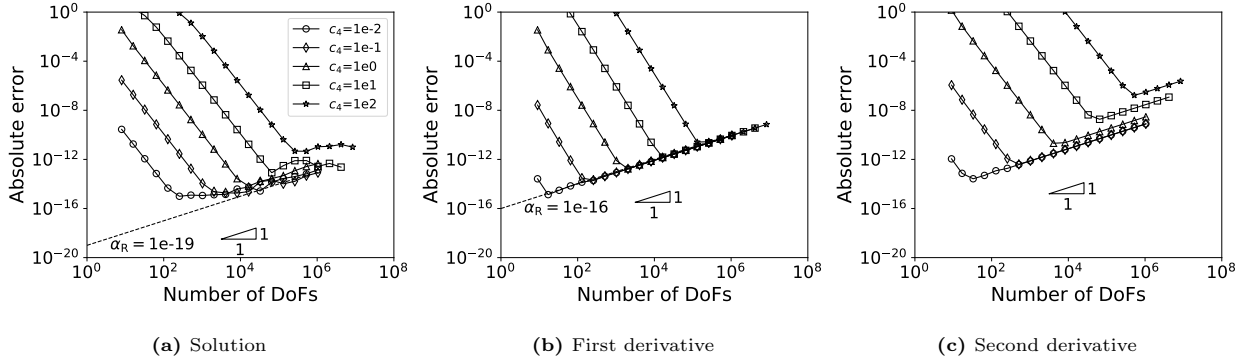


Fig. C.43. Absolute errors for Case 4 in Table 3 using scheme M_2 .

Case 5. For Case 5, using the mixed FEM without scaling the right-hand side and schemes M_1 , the absolute errors are shown in Figs. C.44–C.45.

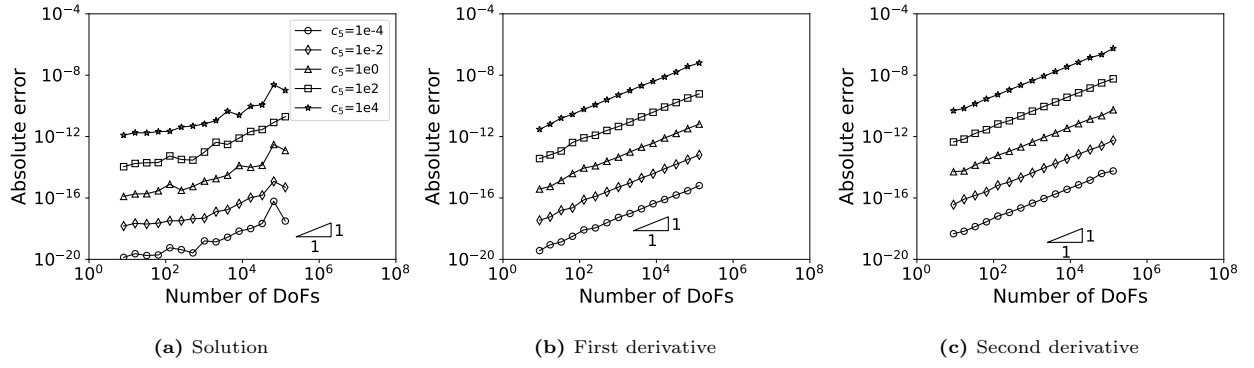


Fig. C.44. Absolute errors for Case 5 in Table 3 using the mixed FEM without scaling the right-hand side.

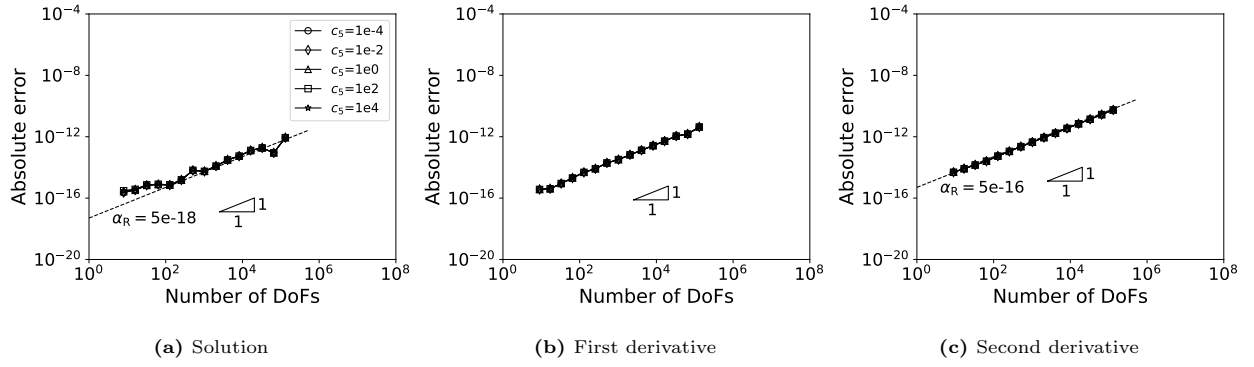


Fig. C.45. Absolute errors for Case 5 in Table 3 using scheme M_1 .

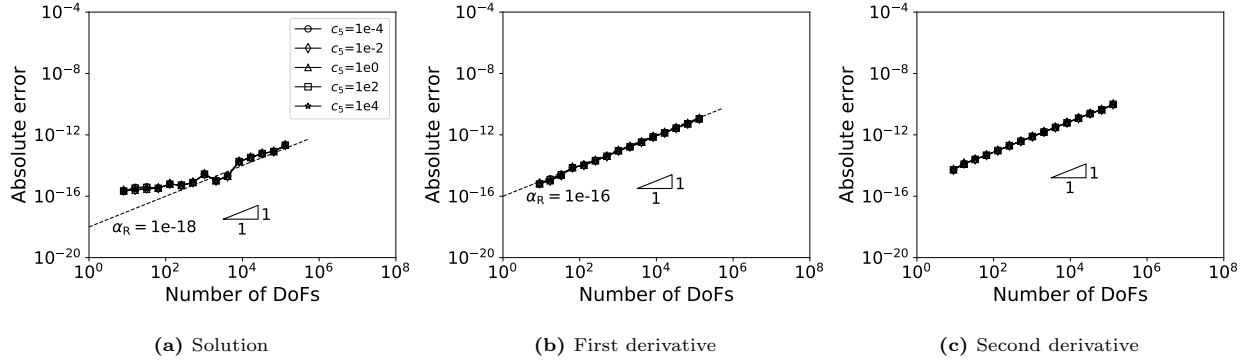


Fig. C.46. Absolute errors for Case 5 in Table 3 using scheme M_2 .

References

- [1] Mohit Kumar, Henk M. Schuttelaars, Pieter C. Roos, and Matthias Möller. Three-dimensional semi-idealized model for tidal motion in tidal estuaries. *Ocean Dynamics*, 66(1):99–118, 2016.
- [2] GF Carey. Derivative calculation from finite element solutions. *Computer Methods in Applied Mechanics and Engineering*, 35(1):1–14, 1982.
- [3] Joel H Ferziger and Milovan Peric. *Computational methods for fluid dynamics*. Springer Science & Business Media, 2012.

- [4] Dan Zuras, Mike Cowlshaw, Alex Aiken, Matthew Applegate, David Bailey, Steve Bass, Dileep Bhandarkar, Mahesh Bhat, David Bindel, Sylvie Boldo, et al. IEEE standard for floating-point arithmetic. *IEEE Std 754-2008*, pages 1–70, 2008.
- 385 [5] Mark S Gockenbach. *Understanding and implementing the finite element method*, volume 97. Siam, 2006.
- [6] B Guo and I Babuška. The hp version of the finite element method. *Computational Mechanics*, 1(1):21–41, 1986.
- [7] Ivo Babuska and Gustaf Söderlind. On roundoff error growth in elliptic problems. *ACM Transactions on Mathematical Software*, 44(3):1–22, 2018.
- [8] Fuyun Ling and J Proakis. Numerical accuracy and stability: Two problems of adaptive estimation algorithms caused by
390 round-off error. In *Acoustics, Speech, and Signal Processing, IEEE International Conference on ICASSP'84.*, volume 9, pages 571–574. IEEE, 1984.
- [9] Shan-Cong Mou, Yu-Xuan Luan, Wen-Tao Ji, Jian-Fei Zhang, and Wen-Quan Tao. An example for the effect of round-off errors on numerical heat transfer. *Numerical Heat Transfer, Part B: Fundamentals*, 72(1):21–32, 2017.
- [10] Mark Ainsworth and J Tinsley Oden. A procedure for a posteriori error estimation for hp finite element methods. *Computer
395 Methods in Applied Mechanics and Engineering*, 101(1-3):73–96, 1992.
- [11] DW Kelly, De SR Gago, OC Zienkiewicz, I Babuska, et al. A posteriori error analysis and adaptive processes in the finite element method: Part I – error analysis. *International Journal for Numerical Methods in Engineering*, 19(11):1593–1619, 1983.
- [12] Daniele Boffi, Franco Brezzi, Michel Fortin, et al. *Mixed finite element methods and applications*, volume 44. Springer,
400 2013.
- [13] Giovanni Alzetta, Daniel Arndt, Wolfgang Bangerth, Vishal Boddu, Benjamin Brands, Denis Davydov, Rene Gassmöller, Timo Heister, Luca Heltai, Katharina Kormann, et al. The deal.II library, version 9.0. *Journal of Numerical Mathematics*, 26(4):173–183, 2018.
- [14] Timothy A Davis. Algorithm 832: UMFPACK V4.3 – an unsymmetric-pattern multifrontal method. *ACM Transactions
405 on Mathematical Software (TOMS)*, 30(2):196–199, 2004.
- [15] Olof Runborg. Lecture notes in numerical solutions of differential equations (dn2255): Verifying numerical convergence rates, 2012.
- [16] Meshing considerations for linear static problems. <https://www.comsol.com/blogs/meshing-considerations-linear-static-problems/>. Accessed: 2019-12-9.
- 410 [17] W Kahan. Floating-point tricks to solve boundary-value problems faster. *University of California@ Berkeley*, 2013.
- [18] Theo Ginsburg. The conjugate gradient method. *Numer. Math.*, 5(1):191–200, December 1963.
- [19] Yuri Bazilevs and Thomas JR Hughes. Weak imposition of Dirichlet boundary conditions in fluid mechanics. *Computers & Fluids*, 36(1):12–26, 2007.